ABSTRACT

Title of Dissertation:	STRONG OPTICAL NONLINEARITY AND SPIN CONTROL WITH PHOTONIC STRUCTURES
	Harjot Singh, Doctor of Philosophy, 2023
Dissertation directed by:	Prof., Edo Waks, Electrical and computer engineering

Photons are excellent carriers of quantum information. Since they hardly interact with each other, they can maintain their quantum state over long distances. However, this poses a challenge if one wishes to create entanglement between the degrees of freedom of photons. Creating entangled states of photons is essential for quantum information processing with photons.

One way to create interactions between photons is to create strong interactions between two level atoms and modes of electromagnetic radiation. This can be achieved by coupling optical transitions of two-level atoms with modes of optical cavities or waveguides. The nonlinearity of a two-level atom then effectively mediates interactions between two (or more) photons. However, due to a fundamental time-bandwidth limit, a two-level atom cannot enable arbitrary quantum operations on the states of two photons.

In this thesis, we study theoretically the problem of splitting two indistinguishable photons to distinguishable output modes with a two-level atom. Due to the time-bandwidth limit, the achieved

splitting efficiency is fundamentally limited to 82% using just a two-level atom. We show that a linear optical unitary transformation on the output modes of the two-level atom can exceed this limit. Via optimization of the input two photon wavefunction and the parameters of the linear optical unitary, we calculated a splitting efficiency of 92%.

For experimental realization of strong atom-light interactions, we used InGaAs quantum dots coupled to a bullseye cavity. Bullseye cavities are promising towards realization of efficient collection of light due to their near Gaussian far field emission. We demonstrated a strong interaction between the quantum dot exciton and the Bullseye cavity mode, quantified by a Cooperativity of ~8. This high cooperativity with a low-quality factor cavity can be attributed to the charge stabilization enabled by the diode heterostructure of the quantum dot samples we used. Finally, we focus on the electron spin ground states of a negatively charged InGaAs quantum dot. The electron spin interacts with the nuclear spins of the In, Ga and As. We measure the spectrum of this interaction using all optical dynamical decoupling pulse sequencies. This work lays a path forward to realizing efficient and coherent spin-photon interfaces with InGaAs quantum dots.

STRONG OPTICAL NONLINEARITY AND SPIN CONTROL WITH PHOTONIC STRUCTURES

by

Harjot Singh

Dissertation submitted to the Faculty of the Graduate School of the
University of Maryland, College Park, in partial fulfillment
of the requirements for the degree of
Doctor of Philosophy
2023

Advisory Committee:
Professor Edo Waks, Chair
Professor Mohammad Hafezi
Professor Cheng Gong
Professor Julius Goldhar
Professor John Cumings

Dedication

I dedicate this thesis to my family and friends.

Acknowledgements

This thesis exists because photons don't interact with each other. So, I would like to thank photons for keeping to themselves most of the time. And yet, this thesis would not exist if photons did not interact with anything at all. In fact, if they didn't interact with anything, you wouldn't be reading this. I hope that this thesis gives the reader some idea about why we would like to make photons effectively "interact" with each other and how that could be useful for information processing.

My advisor Prof. Edo Waks came up with the sketch of ideas that this thesis followed from. I'm first grateful to him for giving me the opportunity to work on these ideas and being a patient mentor who always gave me the freedom to learn from my own mistakes. Whenever I was struggling to make headway on a problem, he had excellent suggestions, which he made with a clarity of thinking that I still try to emulate. Most of my intuition about photons in optical cavities and their interactions with atoms is due to him.

I would also like to express my appreciation for my committee members, Prof. Mohammad Hafezi, Prof. Cheng Gong, Prof. Julius Goldhar, Prof. John Cumings. I must also thank our collaborators Dr. Allan Bracker and Dr. Samuel Carter for providing us with the quantum dot samples that I used for the experimental work in the thesis and for fruitful discussions.

When I joined the lab, I had no idea of how to align any optics at all. It is only through the patient instruction and guidance of Dr. Demitry Farfurnik that I got to a point where

I could perform optical measurements that constitute this thesis. Over the last three years, he has not only been a mentor and a collaborator, but also a friend, and I can't thank him enough for playing these roles with competence, knowledge and kindness.

When it comes to the tools and tricks of nanotechnology that allowed me to make the on-chip optical cavities, there are so many people I learned from and am thankful for. Dr. Subhojit Dutta, Dr. Zhouchen Luo, Dr. Sabyasachi Barik, Dr. Aziz Karasahin, Dr. Shahriar Aghaeimeibodi, Mustafa Buyukkaya, Sam Harper have all at some point taught me something about nanofabrication of on-chip photonic devices that either solved a problem I had been facing or made me see things in a usefully different way. I would also like to thank the staff of UMD's excellent Nanocenter, Doctors John Abrahams, John Hummel, Tom Loughran, Mark Lecates and Jiancun Rao who worked tirelessly to keep the equipment in excellent condition and always provided the training I needed at their earliest convenience.

Over the years I have spent in the group, I've had so many wonderful colleagues and friends who made this journey worthwhile. I'll especially remember the long conversations I had with Dr. Robert Pettit, who's not only an exceptional scientist but also had great life advice to share whenever I needed it. I will always have fond memories of the experiences I shared with with Doctors Subhojit Dutta, Sabyasachi Barik, Aziz Karasahin, Jasvith Basani and Uday Saha both inside and outside of the lab. Special thanks to Dr. Changmin Lee, who was a great office mate for most of my time in the group. I would also like to thank all the other past and present members of the Edo Waks group who I overlapped with: Abhijit Biswas, Bradley Kerkhof, Mustafa Buyukkaya, Sam Harper, Yuqi Zhao, Xinyuan Zheng, Dr. Shahriar Aghaeimeibodi,

Dr. Hamidreza Chalabi, Dr. Young Min Kim, Dr. Zhouchen Luo. Thank you all for being wonderful colleagues and friends.

My roommates over the years I have spent in College Park have all supported me through my research in their own different ways. I would like to especially thank Michael Allen Newman, Christeallia Amorosi, Todd Waters, Katie Reding and Edgar Perez for being the best roommates one could ask for. You all made College Park seem like home.

Some of my friends outside of the research group have given me an unusual amount of support whenever I needed it. Among them, I am especially grateful for Dr. Siddharth Kumar Gururani, Dr. Avik Dutt, Dr. Sumit Mohanty, Sarthak Subhankar, and Yash Deo. My experience inside and outside of the lab through the PhD program was enriched by their presence in my life.

Finally, my family is just awesome. I hope that I get to see all of them soon.

Table of Contents

List of Figures

List of Abbreviations

TLA	Two Level Atom
MZI	Mach Zehnder Interferometer
SEM	Scanning Electron Microscope
EBL	Electron Beam Lithography
QED	Quantum Electrodynamics
DIT	Dipole Induced Transparency
CPMG	Carr-Purcell-Meiboom-Gill
QD	Quantum Dot
FDTD	Finite Difference Time Domain

Chapter 1: Introduction

Photons hardly interact with each other. This is a great feature as far as communication of quantum information is concerned. As a result of the lack of photon-photon interactions, individual photons can preserve their quantum state over long distances in optical fibers. However, if one wants to create quantum correlations aka entanglement between the degrees of freedom of photons, lack of interactions between them poses a challenge. Creating entanglement between photons is essential for quantum information processing with photons[1-3].

Photons can be made to effectively interact with each other by using a medium that interacts with photons[3]. Ideally, the interaction of one photon with such a medium changes the properties of the medium such that a second photon sees effectively a different medium. After the second photon interacts with this medium, one or more of its degrees of freedom would be correlated with those of the first photon. The media of interest are, therefore, nonlinear optical media.

One way to create interactions between photons at the single photon level is to use optical nonlinearities which are effective at the single photon level[3]. Bulk optical nonlinearities, such as $\chi^{(2)}$ and $\chi^{(3)}$ media are not suitable because they are too weak to be effective at the single photon level [10-12].

The nonlinearity of a two-level atom (TLA) is effective at the single photon level. Intuitively, this is because the excitation of a TLA with one photon prevents its excitation with another photon. We can create strong interactions between the atomic nonlinearities and the desired modes of electromagnetic radiation using Cavity

Quantum Electrodynamics. However, time-energy uncertainty relations pose fundamental limits on the quantum operations we can perform on the states of two or more photons with a TLA [25-28].

Another way to create effective interactions between photons is to use a lambda system [13]. A lambda system is a three-level system with two metastable ground states. Depending on the ground state the system is in, its exhibits very different response to incoming photons. This difference is leveraged to create perfect entanglement between two photons.

In this thesis, we focus on theoretical as well as experimental aspects of creating photon-photon interactions using a two-level atom. We also perform experiments on a lambda system. Our experimental systems of choice in both cases are InGaAs quantum dot excitons. Uncharged excitons realize an "artificial" two-level atom, and we use negatively charged excitons to obtain a lambda system[102]. The two metastable states of the lambda system are provided by the spin state of the electron. To do cavity quantum electrodynamics with quantum dot excitons, we use electron beam lithography to pattern optical cavities on our quantum dot chips. In the following sections of this chapter, we introduce these different themes that occur throughout this thesis.

1.1 Cavity Quantum Electrodynamics (Cavity QED)

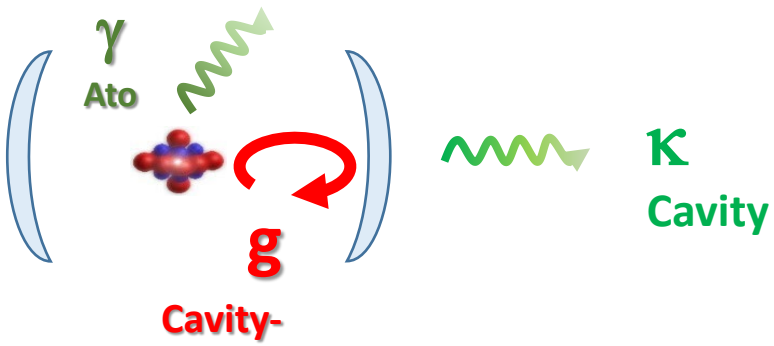

Figure 1: Schematic illustrating the basics of a cavity quantum electrodynamics system.

Figure 1 shows the schematic of a paradigmatic cavity quantum electrodynamics system. Here the two mirrors form an optical cavity. The atom here has two energy levels. The excited state spontaneous decay rate into the vacuum modes of electromagnetic radiation is γ. The coupling rate between the atom and the cavity mode is g. The cavity mode decays out of the mirrors at a rate of κ.

Throughout this thesis, we model the atom-cavity coupling with the Jaynes-Cummings Hamiltonian [102], given by:

$$H_{int} = g(a^{+}\sigma + \sigma^{+}a) \tag{1.1}$$

where σ and σ^{+} are the lowering and raising operators of the TLA with excited state $|e\rangle$ and ground state $|g\rangle$ and a and a^{+} are the excitation and annihilation operators of the cavity mode respectively.

The strength of the interaction between the atom and the cavity mode is said to be strong when the coupling rate g dominates over the two decay rates γ and κ. The

quantity of interest for quantum information processing applications is the cooperativity C given by:

$$C = g^2/\kappa\gamma \tag{1.2}$$

Broadly speaking, the regime of interest is when $C > 1$, which is colloquially known as the regime of strong interaction between light and matter. However, there are some more constraints on the relationship between the different rates $g, \kappa \; and \; \gamma$ which give to qualitatively different physics. These are the strong coupling and the weak coupling regimes of cavity QED which we will describe in the following subsections.

1.1.1 Strong Coupling Regime of Cavity QED

When the interaction rate between the mode of the optical cavity and the atom i.e. g dominates over the leaky rates κ and γ, we are in the strong coupling regime. In this regime, the strong interaction term between the atom and cavity leads to hybridization of the states of the atom and cavity, giving rise to the famous Jaynes-Cummings ladder. Spectrally, this is usually observed as the vacuum Rabi splitting.

1.1.2 Weak Coupling Regime of Cavity QED

Weak coupling regime occurs when $\kappa > g$, and $g \gg \gamma$ such that the cavity mode leaks faster it interacts the atom, but the atom still interacts more strongly with the cavity mode than it does with the vacuum modes of electromagnetic radiation. This regime is also known as the Bad Cavity Regime. In this thesis, we will only concern with the case when the cavity only leaks into the modes that we can collect photons from. For Figure 1, this corresponds to the imperfect reflectivity of the two mirrors being the only source of leakage, such that the photons transmitted by the mirrors can be collected and

measured. This set of conditions was appropriately called the "fast cavity regime" by Rosenblum et. al. [28], as the fast leaking of the cavity is not necessarily bad if it's not leaking into unwanted decay channels.

We further elaborate on the different regimes and aspects of cavity-atom coupling through this thesis depending on the context.

1.2 Cavity QED with a Lambda system

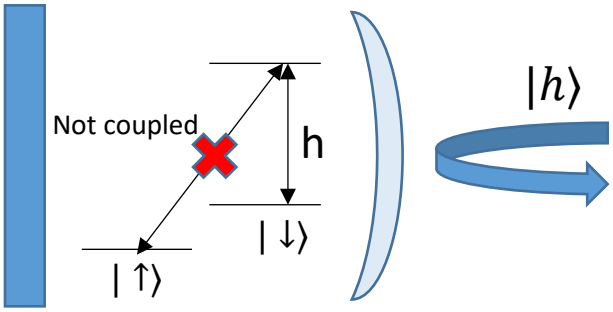

Figure 2 Schematic of a lambda system with one of its optical transitions coupled to the cavity mode.

We consider a lambda system with two metastable ground states, here and throughout this thesis given by the two spin states of an electron. Figure 2 shows such a system coupled to a single sided cavity where the plane mirror is assumed to be 100% reflective. One of the optical transitions is in resonance with and couples to the mode of the cavity, which is h polarized. The other transition couples only to v polarized light and is also far detuned from the cavity mode and therefore doesn't couple to it.

In order to create photon-photon entanglement with this system, we need to coherently control the spin state of the electron [13,98]. We would like to create the superposition state given by $(|\uparrow\rangle + |\downarrow\rangle)/\sqrt{2}$. For this, we need external control of the spin state of the electron, which in most atomic systems is implemented using a direct drive of the

microwave frequency spin transition between $|\uparrow\rangle$ and $|\downarrow\rangle$. As we shall discuss in Chapter 4 of this thesis, direct microwave control of spin states in a charged InGaAs quantum dot exciton is not feasible[59]. Therefore, we use all-optical control, first established in ref. 59, which we will briefly touch upon in a later section of this introduction.

Provided that the cooperativity corresponding to the coupled transition is much greater than 1 and coherent control of the spin states is achieved, it is possible to create perfect entanglement between the polarization states of the two photons [13]. More concretely, it is possible to implement a controlled phase gate between the polarization states of the two photons [13,98]. Given that this gate can be implemented with high fidelity, we can in principle achieve quantum computation with qubits implemented by the two polarization states of photons.

1.3 InAs/GaAs quantum dots

The basic idea behind semiconductor quantum dots is sandwiching a lower bandgap semiconductor between layers of a higher bandgap semiconductor creating a so-called quantum well potential for electrons and holes. Figure 3 illustrates this idea for InAs/GaAs quantum dots. Here InAs, which is the lower bandgap material is sandwiched between GaAs, the higher bandgap material. The red dotted lines denote the discrete energy levels of the quantum well. These levels correspond to bound states that are confined in the 2-dimensional quantum well.

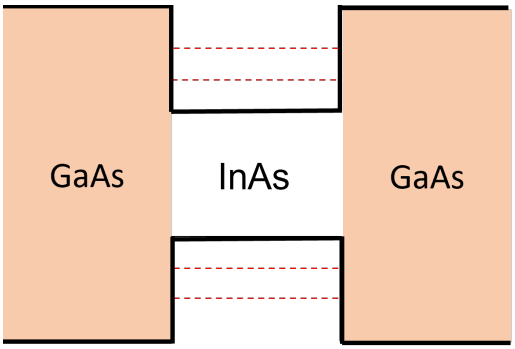

Figure 3 InAs/GaAs quantum well bandstructure

We require three-dimensional confinement of carriers to create the desired two-level atomic system. Fortunately, this happens spontaneously during the MBE growth of the InAs and GaAs using the Stranski-Krastanov (SK)) method [92,102]. Figure 4 shows a scanning electron microscope (SEM) image of the cross-section of the grown materials using this method.

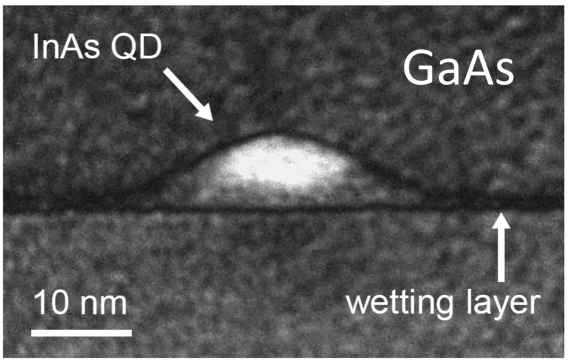

Figure 4 SEM image illustrating the formation of InAs quantum dots.

Due to the strain caused by lattice mismatch between GaAs and InAs, islands of InAs dots are formed during the growth of InAs on top of GaAs. This results in an effective three-dimensional confinement of excitons in these dots, giving us the desired two-level systems. When an extra electron is trapped inside this dot, the dot has two metastable ground states given by the spin up and down states of the electron. This

creates a lambda system, which can be used to create a controlled phase gate between the polarization states of photons.

1.4 Making cavities on chip: Photonic crystals.

To perform cavity QED with InAs quantum dots, which is required for obtaining single photon nonlinearity, we pattern the so-called photonic crystal cavities on the MBE grown quantum dot wafers using Electron Beam Lithography (EBL) [102]. We will describe the details of this fabrication process in Chapter 3 with the example of the fabrication of the circular Bragg grating aka Bullseye cavities.

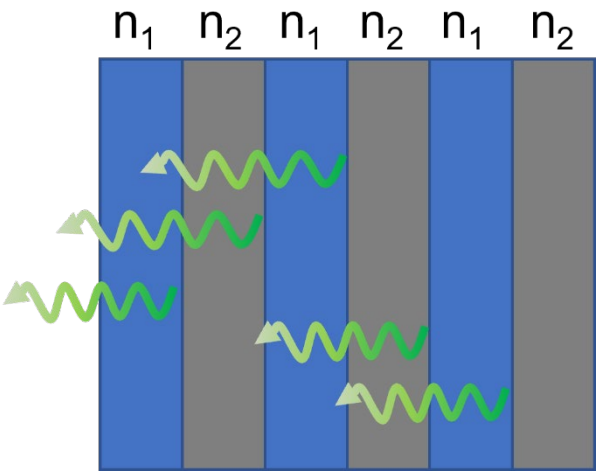

Figure 5: Principle of photonic crystals: Bragg reflection by refractive index modulation

To create on-chip mirrors for optical cavities, we use the idea of Bragg interference caused by refractive index modulation. This refractive index modulation is done periodically, hence the name photonic crystals. Figure 5 illustrates this basic idea. There is partial reflection and transmission of light at every interface between media of the two different refractive indices n_1 and n_2. Depending on the periodicity of the modulation, the reflections at different interfaces constructively interfere only at certain wavelengths. The illustrated photonic crystal acts as a mirror for those wavelengths.

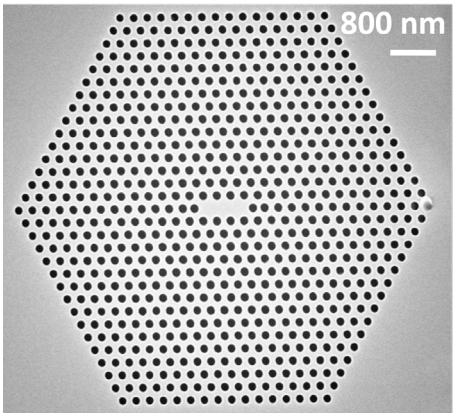

Figure 6 Leaving out three holes from the hexagonal lattice photonic crystal to form the L3 cavity

For our experiments with InAs quantum dots, we achieve this refractive index modulation by periodically punching holes through our chip or forming gratings. One way of forming photonic crystal cavities is to leave some defects in the photonic crystal formed by a periodic array of holes. Figure 6 illustrates this idea by the way of the example of L3 cavities where this defect region is formed by leaving 3 holes out of the photonic crystal. This defect can be seen as being surrounded by mirrors from all sides. Therefore, the modes of the cavity formed by this photonic crystal cavity is confined in the defect region.

1.5 Experimental setup and measurement tools.

1.5.1 Polarization resolved confocal microscope for cryogenic measurements.

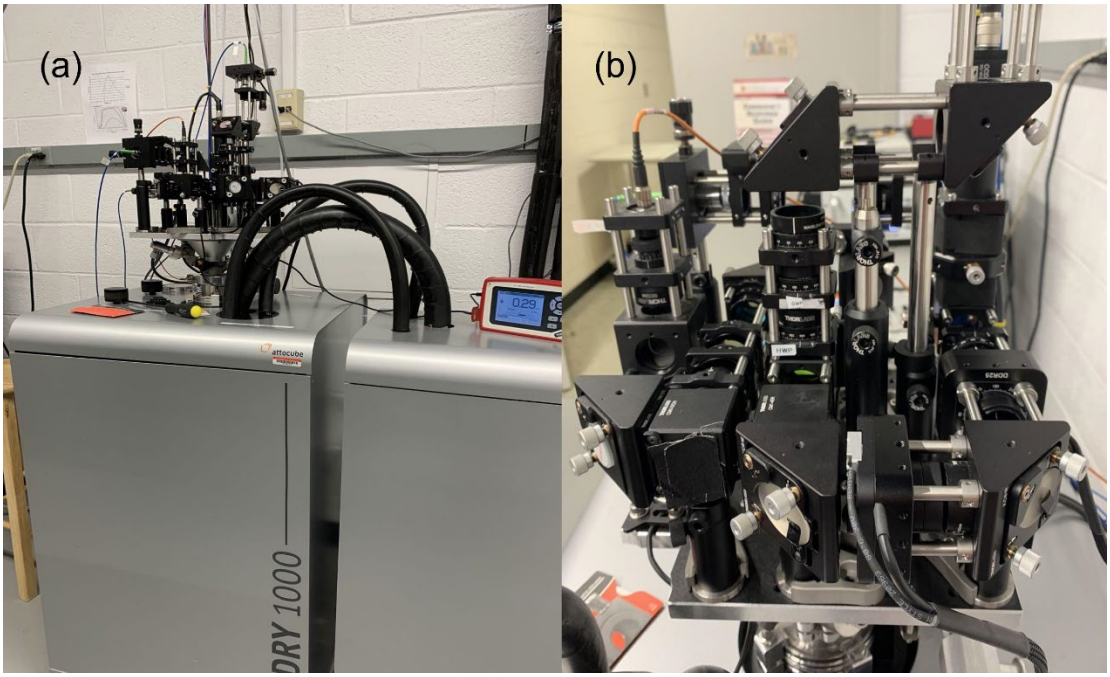

Figure 7(a) Helium exchange gas cryostat with the sample inside and an optical breadboard on top (b) a close up of the optical breadboard which forms part of a confocal microscope.

Figure 7 shows a part of our experimental setup including a Helium exchange gas cryostat and the optical breadboard on top of it. We place our quantum dot samples inside the cryostat to preserve the quantum coherence of the quantum dot excitons as well as the electron spin. The optics on top of the optical breadboard forms a part of a confocal microscope. The objective lens of the microscope inside the cryostat.

As shown in Figure 7(b), a key feature of our confocal microscope is the ability to manipulate the polarization of light over the entire Poincare sphere. This allows us to perform cross-polarized measurements, where we collect light polarization which is orthogonal to the polarization of the excitation light. This gets rid of the excitation light

background, such that we are only collecting photons emitted by the quantum dot exciton in a resonance fluorescence measurement.

1.6 Thesis Outline

In Chapter 2, we provide a comprehensive analysis of our theory results on improving photon-photon splitting beyond the limitations of the nonlinearity of a two-level atom. Using linear optical transformation on the output modes of the atom, we derive an optimal input wavefunction which gives a routing efficiency of 92%. In comparison, the previously known limit using the bare two-level atom is 77%.

In Chapter 3, we briefly review the relevant developments in the field of InAs/GaAs quantum dots. We mainly discuss the work on diode heterostructures and their importance in improving the properties of InAs/GaAs quantum dots. We focus on pinin diode heterostructures, compare them with other heterostructures and explain why we choose to focus on them in this thesis. We also present the result from the work on all optical noise spectroscopy of dots in pinin heterostructures, to which the author of this thesis made secondary contributions. For this work, pinin heterostructures were sandwiched between two (Distributed) Bragg mirrors of the type described in section 1.4 to form a so called double DBR (distributed Bragg reflector) cavity.

In Chapter 4, we demonstrate strong interactions between a quantum dot exciton and the mode of a Bullseye cavity. By simulating the quantum dynamics of the system using QuTiP in python, we extract a Cooperativity of ~8. By performing time-resolved measurements of the quantum dot emissions, we demonstrate a Purcell Enhancement of 15.

In Chapter 5, we show the experimental developments towards performing cavity QED with nanobeam cavities. We show the novel developments in fabrication processes required to fabricate nanobeam cavities and show some preliminary data from the optical measurements of the nanobeam cavities at room temperature. These devices are designed to couple very efficiently to lensed fibers. We will discuss why we need high optical efficiencies for applications in quantum information processing and the future developments required to achieve the same.

Parts of this thesis have been published in the following journal articles:

1.) Singh, H., Farfurnik, D., Luo, Z., Bracker, A. S., Carter, S. G., & Waks, E. (2022). Optical Transparency Induced by a Largely Purcell Enhanced Quantum Dot in a Polarization-Degenerate Cavity. Nano Letters, 22(19), 7959-7964.

2.) Farfurnik, D., Singh, H., Luo, Z., Bracker, A. S., Carter, S. G., Pettit, R. M., & Waks, E. (2021). All-optical noise spectroscopy of a solid-state spin. Nano Lett. 2023, 23, 1781−1786.

Chapter 2: Splitting indistinguishable photons beyond the blockade limit via linear optics.

2.1 Introduction

Paradigms for quantum computing and networks have proposed the use of photons as the substrate for quantum information processing. Hardware driven by photonics has enjoyed success in a multitude of applications ranging from machine learning [1–4] to quantum communication networks [5, 6] and simulation [7–12]. The lack of direct interactions between photons and the environment thus make them robust carriers of quantum information, immune to decoherence. Conversely, this absence of direct interactions pose a significant challenge for realizing universal quantum operations on quantum states of multiple photons. To enable the full range of envisioned applications, a challenge of central importance is to generate and engineer strong photon-photon interactions.

Optical nonlinearities that indirectly mediate interactions between photons have been deemed as a viable route to realize such photon-photon coupling. Bulk optical nonlinearities are an attractive option due to their potential for room temperature operation, but at this stage are still too weak [13–15]. Alternatively, by coupling these photons to an ancillary quantum system, strong nonlinearities can be engineered. One such candidate is the Two-Level Emitter (TLE) coupled to a cavity or a waveguide [16, 17], which leverages strong light-matter interactions to mediate interactions between photons [18, 19]. The nonlinear response of TLEs has been well studied [20–22] and has been realized experimentally using quantum dots [23, 24], atoms [25, 26], ions [27]

and superconducting circuitry [28]. However, it has been widely accepted that the interactions mediated by a TLE suffer from time-bandwidth trade-offs implied by time-energy uncertainty. These trade-offs have been shown to impose fundamental constraints on the fidelity of operations such as CPHASE gates [29], photon sorting [30, 31] and photon routing [32].

One application of interest is photon-photon splitting, where two or more indistinguishable photons incident on the TLE via a single channel are routed into two or more output channels [33]. Linear optical unitaries have been shown to reach peak routing efficiencies of only 50%. Leveraging the photon blockade effect of a two-level atom (where its excitation by one photon prevents its excitation with another photon), on the other hand, is known to exceed this limit. The use of the photon blockade effect is, however, still insufficient to achieve perfect routing due to the time-bandwidth trade-off [30, 32, 34]. An extensive analysis for the routing of two-photons limited by the time-bandwidth trade-off has been performed in ref. [32], where peak routing efficiencies of 64% and 68% were attained for pulses with Lorentzian and Gaussian spectral profiles respectively. Engineering the time-energy relations by adding entanglement between the input photons further improves this efficiency, but the splitting efficiency is still limited to 77% for an entangled pulse with a Lorentzian spectral profile.

In this chapter, we show that the blockade limited routing efficiency can be exceeded with the use of a linear optical unitary transformation after the atom. We optimize the unitary to achieve the best routing efficiency for an uncorrelated two-photon input and show that it can exceed 82% for a Gaussian pulse shape. We subsequently show that

time- energy entangled inputs can achieve routing efficiencies exceeding 90%. Finally, we optimize the entangled photon wavefunction to achieve an optimal routing efficiency of 92%. This efficiency is significantly larger than the limit set by a two-level emitter alone with no unitary. In all cases, the unitary transformation fundamentally changes the time-bandwidth trade-off, resulting in optimal performance at a reduced bandwidth of the input pulse compared to the bare two-level emitter.

This chapter is organized as follows: In section 2 we derive the most general time-domain solutions for the probabilities of scattering event for two-photon wavepackets incident on the two-level emitter and Mach-Zehnder Interferometer system. In section 3 we find the optimal unitaries that maximize the routing efficiency for both entangled and unentangled photons. In section 4, we additionally optimize the temporal wavefunction of the entangled photon input to achieve a more optimal routing efficiency than would be possible by standard exponential or Gaussian temporal modes. Finally, section 5 concludes the chapter with a further discussion of the scope and impact of the results described in this chapter.

2.2 System Model and Method

Fig. 8(a) shows the standard approach to single photon routing using a two-level emitter. The system is composed of a two-level emitter coupled to a waveguide. The 2 modes $\mathbf{a}_{in}$ and $\mathbf{b}_{in}$ are inputs to the emitter and $\mathbf{a}_{out}$ and b_{out} are the output modes. In the photon routing scenario, two photons are injected from mode $\mathbf{a}_{in}$ and scatter into the two output modes. Mode $\mathbf{b}_{in}$ is in the vacuum state. Fig. 8(b) shows another way to implement this system, where a two-level emitter is coupled to a double-sided cavity. These two systems are equivalent in the bad cavity limit ($\gamma \ll \kappa$) where γ represents the

two-level emitter's spontaneous emission rate and κ denotes the cavity decay rate. In this limit, the cavity atom system can be replaced by a one-dimensional atom model with a modified spontaneous emission rate given by $\gamma = 4g^2/\kappa$ [35], where g is the atom-cavity coupling strength.

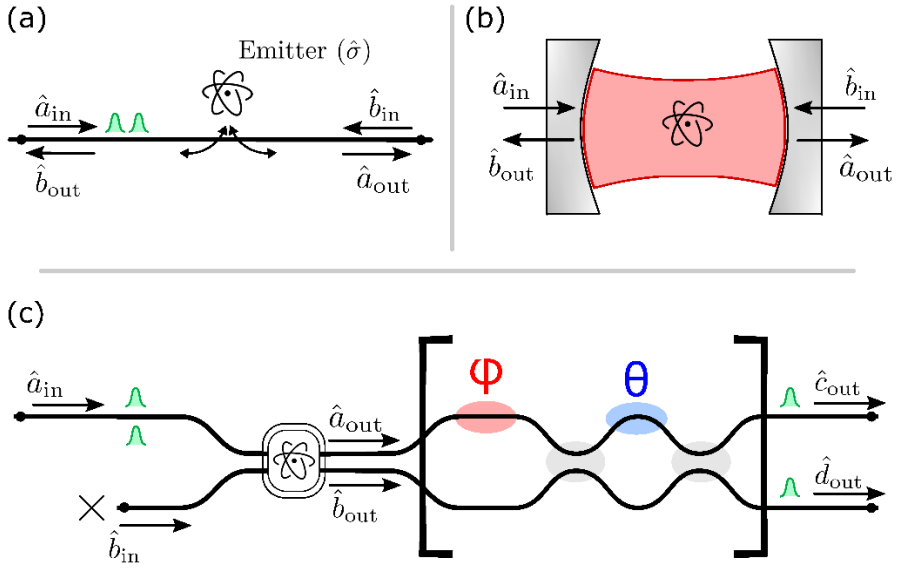

Figure 8 (a) Schematic of two-level emitter coupled to a waveguide, indicating the directions of the input and output modes. (b) Alternative implementation using an atom coupled to a double-sided cavity. (c) Schematic for the photon router, where the output modes of the two-level emitter are injected into a Mach-Zehnder Interferometer.

Due to photon blockade, the two input photons may be routed to spatially distinguishable output modes $\mathbf{a_{out}}$ and $\mathbf{b_{out}}$, an effect which we refer to as photon splitting. We define the photon splitting efficiency as the probability that two photons in the same input port exit at different output ports. Rosenblum et al. extensively analyzed the splitting efficiency of a single atom and showed it was limited to 77% due to a time-bandwidth tradeoff [28].

To improve the splitting efficiency, we consider the system in Fig. 8(c). We place a Mach-Zehnder Interferometer after the atom which applies a general linear optical unitary transformation given by:

$$\begin{bmatrix} \hat{c}_{\text{out}} \\ \hat{d}_{\text{out}} \end{bmatrix} = \begin{bmatrix} e^{i\phi}\sin(\theta/2) & \cos(\theta/2) \\ e^{i\phi}\cos(\theta/2) & -\sin(\theta/2) \end{bmatrix} \begin{bmatrix} \hat{a}_{\text{out}} \\ \hat{b}_{\text{out}} \end{bmatrix} \tag{2.1}$$

In the above equations, $\mathbf{c_{out}}$ and $\mathbf{d_{out}}$ are the output modes of the unitary, which are directly related to the input modes via a scattering matrix. The scattering matrix has two tunable parameters, θ and ϕ, which are represent applied phase shifts as shown in the figure. By tuning these two parameters we can implement any desired two-mode unitary transformation. We will use these two parameters to optimize the splitting efficiency into the output modes.

To calculate the routing efficiency after the interferometer, we first define the time-ordered second order correlation functions:

$$\Gamma^{\text{pq}}(\tau_1, \tau_2) = \langle \psi_o | \, \hat{p}^{\dagger}_{\text{out}}(\tau_1)\hat{q}^{\dagger}_{\text{out}}(\tau_2)\hat{q}_{\text{out}}(\tau_2)\hat{p}_{\text{out}}(\tau_1) \, | \psi_o \rangle \tag{2.2}$$

where {p, q} ∈ {c, d}. These correlations represent the probability densities that a photon is detected at time τ_1, and a second photon is detected at time τ_2. The wavefunction $|\psi_0\rangle$ represents the initial state of the system, which is assumed to be in the subspace where both photons are in mode $\mathbf{a_{in}}$ and the atom is in the ground state. Because these are time-ordered correlations it is implicit that $\tau_2 \geq \tau_1$ in all calculations. Because we are restricting our attention only to a two photon input, the correlations can be written as $\Gamma_{pq}(\tau_1, \tau_2) = |\psi_{pq}(\tau_1, \tau_2)|^2$ where $\psi_{pq}(\tau_1, \tau_2)$ is the correlation amplitude given by:

$$\psi_{\mathrm{pq}}(\tau_1,\tau_2) = \langle 0|\, \hat{q}_{\mathrm{out}}(\tau_2)\hat{p}_{\mathrm{out}}(\tau_1)\, |\psi_0\rangle \tag{2.3}$$

From these correlations, we can directly calculate the splitting efficiency P_S as:

$$P_S = \int \mathrm{d}\tau_1 \int \mathrm{d}\tau_2 \left[\Gamma^{\mathrm{cd}}(\tau_1,\tau_2) + \Gamma^{\mathrm{dc}}(\tau_1,\tau_2)\right] \tag{2.4}$$

To calculate the routing efficiency, we apply the unitary to derive a relation between the correlation ψ_{cd} and ψ_{dc} in terms of the correlation amplitudes of the outputs of the atom given by:

$$\psi_{\mathrm{lm}} = \langle 0|\, \hat{m}_{\mathrm{out}}(\tau_2)\hat{l}_{\mathrm{out}}(\tau_1)\, |\psi_0\rangle \tag{2.5}$$

where in the above {l, m} ∈ {a, b}. The above amplitudes are related to the output amplitudes of the interferometer via the relations:

$$\begin{aligned}\psi_{\mathrm{cd}} = {} & e^{-2i\phi}\sin(\theta/2)\cos(\theta/2)\psi_{\mathrm{aa}} - e^{-i\phi}\sin^2(\theta/2)\psi_{\mathrm{ab}} + \\ & e^{-i\phi}\cos^2(\theta/2)\psi_{\mathrm{ba}} - \sin(\theta/2)\cos(\theta/2)\psi_{\mathrm{bb}} \qquad (2.6a)\\ \psi_{\mathrm{dc}} = {} & e^{-2i\phi}\sin(\theta/2)\cos(\theta/2)\psi_{\mathrm{aa}} + e^{-i\phi}\cos^2(\theta/2)\psi_{\mathrm{ab}} - \\ & e^{-i\phi}\sin^2(\theta/2)\psi_{\mathrm{ba}} - \sin(\theta/2)\cos(\theta/2)\psi_{\mathrm{bb}} \qquad (2.6b)\end{aligned}$$

The above expressions enable us to directly calculate the output correlations of the interferometer from the correlation amplitudes of the atomic output modes.

To calculate the correlation amplitudes of the atomic output modes, we use the standard Hamiltonian for the interaction of an atom with a waveguide given by H = $H_0 + H_{int}$ where [16, 36]:

$$\hat{H}_0 = \int_{-\infty}^{\infty} d\omega\, \omega(\hat{a}_\omega^\dagger \hat{a}_\omega + \hat{b}_\omega^\dagger \hat{b}_\omega) \tag{2.7}$$

and

$$\hat{H}_{\text{int}} = -i\sqrt{\frac{\gamma}{\pi}}\int_{-\infty}^{\infty} d\omega\,[\hat{\sigma}^{\dagger}(\hat{a}_{\omega}+\hat{b}_{\omega}) - \hat{\sigma}(\hat{a}_{\omega}^{\dagger}+\hat{b}_{\omega}^{\dagger})] \tag{2.8}$$

In the above equations, **σ** is the atomic lowering operator and $\mathbf{a}_{\omega}$ are the bosonic reservoir mode operators for the waveguide. They are related to the input modes via the relation $a_{in}(\omega) = 1/\sqrt{2\pi}\int dt\, a_{in}(t)e^{-i\omega t}$. The input and output modes are also directly related to each other by the input-output relations $\mathbf{a}_{out} = \mathbf{a}_{in} - \sqrt{2\gamma}\boldsymbol{\sigma}$ and $\mathbf{b}_{out} = \mathbf{b}_{in} - \sqrt{2\gamma}\boldsymbol{\sigma}$ [16].

As we feed the input pulse through $\mathbf{a}_{in}$, $\mathbf{b}_{in}$ is only a vacuum noise input. Since, we are calculating normally ordered moments of output operators, vacuum noise inputs from both input ports can be ignored and we can rewrite $\mathbf{b}_{out} = \sqrt{2\gamma}\boldsymbol{\sigma}$. The initial state of the two photons in the input channel $\mathbf{a}_{in}$ can be written as:

$$|\psi_0\rangle = \int_{-\infty}^{\infty} \mathrm{d}t_1 \int_{t_1}^{\infty} \mathrm{d}t_2\; \xi(t_1,t_2)\hat{a}_{\text{in}}^{\dagger}(t_1)\hat{a}_{\text{in}}^{\dagger}(t_2)\,|0\rangle\,|g\rangle \tag{2.9}$$

In Appendix 2.A, we show that the output correlation amplitudes after the atom are given by:

$$\psi_{\text{bb}}(\tau_1,\tau_2) = 4\gamma^2 e^{-2\gamma(\tau_1+\tau_2)}\left(\int_{\tau_1}^{\tau_2}\mathrm{d}t_2\int_{-\infty}^{\tau_1}\mathrm{d}t_1\; e^{2\gamma(t_1+t_2)}\xi(t_1,t_2)\right) \tag{2.10a}$$

$$\psi_{\text{ba}}(\tau_1,\tau_2) = -2\gamma e^{-2\gamma\tau_1}\left(\int_{-\infty}^{\tau_1}\mathrm{d}t_1\; e^{2\gamma t_1}\xi(t_1,\tau_2)\right) + \psi_{\text{bb}}(\tau_1,\tau_2) \tag{2.10b}$$

$$\psi_{\text{ab}}(\tau_1,\tau_2) = -2\gamma e^{-2\gamma\tau_2}\left(\int_{-\infty}^{\tau_1}\mathrm{d}t_1\; e^{2\gamma t_1}\xi(t_1,\tau_1) + \int_{\tau_1}^{\tau_2}\mathrm{d}t_2\; e^{2\gamma t_2}\xi(\tau_1,t_2)\right) + \psi_{\text{bb}}(\tau_1,\tau_2) \tag{2.10c}$$

$$\psi_{\text{aa}} = \xi(\tau_1,\tau_2) + \psi_{\text{ab}}(\tau_1,\tau_2) + \psi_{\text{ba}}(\tau_1,\tau_2) - \psi_{\text{bb}}(\tau_1,\tau_2) \tag{2.10d}$$

With these expressions for the two photon correlation amplitudes in the output modes of the emitter, we can directly calculate the photon splitting efficiency in eqn. (2.6) and eqn. (2.4).

2.3 Results

2.3.1 Routing Unentangled Photons

We first analyse the routing efficiency for an input of two unentangled photons. In this case we can write the wavefunction as $\xi(t_1, t_2) = \sqrt{2}\,\xi(t_1)\xi(t_2)$. Here ξ(t) is a normalized single photon wavepacket and the factor of $\sqrt{2}$ ensures that the input state is normalized under time-ordering $t_1 \geq t_1$ [11]. We analyze two pulse profiles for the single photon input wavepackets. The first is an exponential pulse profile such that $\xi(t) = \sqrt{2\kappa}e^{-\kappa t}$, and the second is a gaussian pulse profile given by $\xi(t)\left(\sqrt{\frac{2}{\pi}}\kappa\right)^{\frac{1}{2}} e^{-\kappa^2 t^2}$. In both cases κ parametrizes the bandwidth of the pulse.

We calculate the routing efficiency using the results of the previous section. In Appendix 2.C, we perform the full calculation for the exponential wavepacket, which leads to an analytical solution. For the Gaussian pulse it is not possible to attain an analytical expression, so we numerically calculate the routing efficiency. Figures 9(a) and 9(b) plot the resulting routing efficiency as a function κ and θ for uncorrelated inputs with Gaussian and Exponential pulse profiles respectively. Since the routing efficiency has a periodicity in θ of π/2, we analyze and plot only one period. For each point on the plot, we optimize the value of the interferometer input phase φ (see fig. 8) to obtain the maximum splitting efficiency for the values of θ and κ corresponding to that point. We find that φ = 0 optimizes the splitting efficiency for all points with θ ≤

$\pi/4$ and $\varphi = \pi$ optimizes the splitting efficiency for $\theta > \pi/4$. This is true for both exponential and gaussian pulses. Furthermore, the splitting efficiency optimized for φ is mirrored across the line $\theta = \pi/4$, such that the value at θ is the same as the value at $\pi/2 - \theta$, where $\theta < \pi/4$.

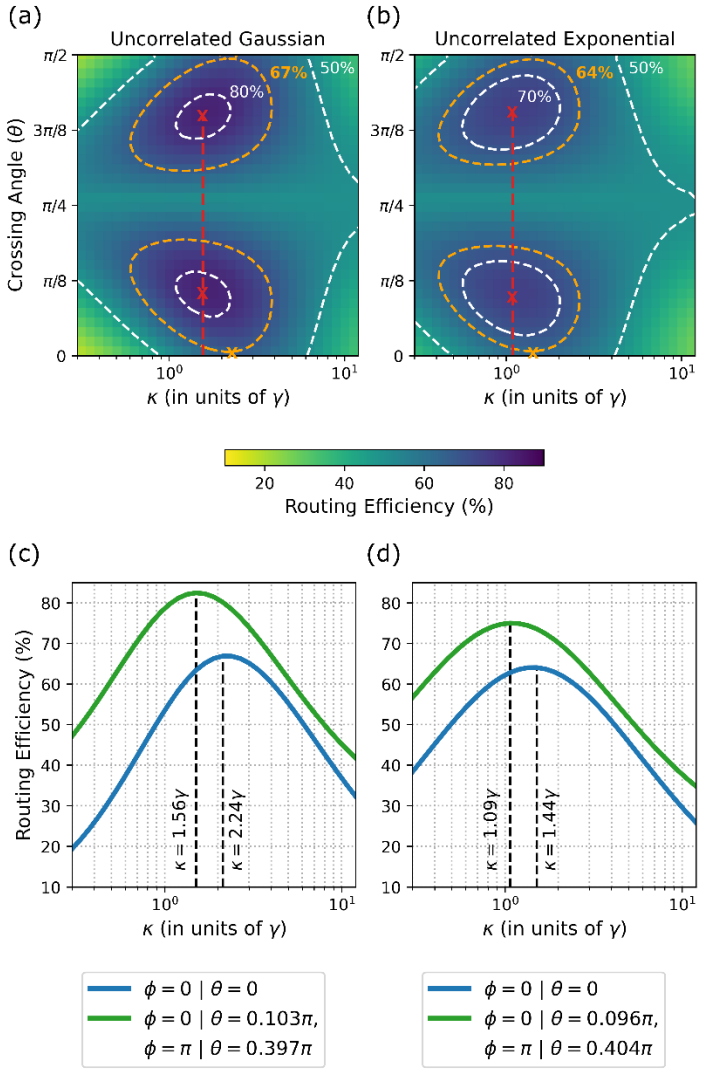

Figure 9 Routing efficiency for unentangled inputs (see text for details)

The red dot denotes the maximum splitting efficiency in both plots, which is obtained at (θ, φ) values of (0.103π, 0) for the gaussian wavepacket and (0.096π, 0) for the

exponential wavepacket. As we noted in the last paragraph, there are values of $\theta > \pi/4$ which result in the same optima when the phase difference φ between the two input arms of the interferometer is set to π. The orange contours represent the bare atom routing efficiency calculated in ref. [28] for a Gaussian wavepacket (67%) and exponential wavepacket (65%). One can see that the red dot in both cases is within these orange contours and therefore achieves a higher routing efficiency.

We next compare the optimal splitting efficiency obtained with the Mach-Zehnder interferometer to that of the bare atom. We can extract the bare atom routing efficiency from the $\theta = 0$ cross-section of the plots in figures 9(a) and 9(b). In this case the unitary implements the identity transformation and we therefore recover the bare atom response. Figs. 9(c) and 9(d) plot the splitting efficiency as a function of the input pulse bandwidth for these two unitary transformations. The blue curves correspond to having no unitary on the outputs of the atom, and give the blockade limited efficiency. The green curves corresponds to the unitary transformation that optimizes the splitting efficiency. For the exponential pulse, the blockade limited efficiency is 65% and occurs at $\kappa = 1.44\gamma$. In contrast, the optimal splitting efficiency with the unitary is 0.75. The bandwidth κ which achieves this global maximum is 1.09γ, is therefore smaller than the optimal bandwidth which achieves the blockade limited efficiency. For the Gaussian pulse, optimal bandwidth κ is 1.57γ, which achieves an optimal splitting efficiency of 82%. This efficiency is larger than the blockade limited efficiency of 0.67. We achieve this optimal at a smaller than that realized by the bare atom, which is 2.24γ for a Gaussian input pulse. Therefore, the unitary transformation fundamentally changes the time-bandwidth trade-off required to achieve optimal splitting efficiency.

2.3.2 Routing time-energy entangled photons

We now analyze the response of our system for in- puts which are time-energy entangled. These inputs have time-energy uncertainty relations which are fundamentally different from the uncorrelated inputs. Therefore, their interaction with the two-level atom is also different. One way to write a time-energy entangled photon state is as follows:

$$|\psi\rangle = \int \mathrm{d}\omega_0 \; G(\omega_0) \int \mathrm{d}\omega \; F(\omega) \, |\omega, \omega_0 - \omega\rangle \tag{2.11}$$

where $G(\omega_o)$ and $F(\omega)$ are general wavefunctions constrained only by the requirement for the overall normalization of the state. The above wavefunction can be expressed in the time domain as:

$$|\psi\rangle = \int \mathrm{d}t_1 \; g(t_1) \int \mathrm{d}t_2 \; f(t_2 - t_1) a^\dagger(t_1) a^\dagger(t_2) \, |0\rangle \tag{2.12}$$

where $g(t_1)$ and $f(t_2 - t_1)$ are Fourier transforms $G(\omega_o)$ and $F(\omega)$. In the limit where $G(\omega_0) = \delta(\omega_0)$, we then have $g(t_1) = 1/2\pi$ which achieves a perfect temporally correlated entangled state which depends only on the time difference $t_2 - t_1$. We refer to such states as stationary, because the correlations only depend on the arrival time difference, and do not depend on the values of the individual time variables. A more general entangled state can introduce non-stationary behavior where correlations are time-dependent, with the dependence quantified by the function $g(t_1)$.

We first consider the specific case where $g(t_1) = \sqrt{2\kappa}\, e^{-\kappa t_1}$ and $f(t2 \; - \; t1) \; =$

$\sqrt{2\delta}e^{-\delta(t_2-t_1)}$. Here the two wavefunctions are exponential where κ and δ represent the bandwidths of the respective distributions. We attain the stationary limit when κ →0. From this state, we obtain the following normalized input wavefunction:

$$\xi(t_1,t_2) = 2\sqrt{\kappa\delta}\; e^{-\kappa t_1} e^{-\delta(t_2-t_1)} \tag{2.13}$$

where $\xi(t_1, t_2)$ is defined in eqn. (9). We begin with the above input wavefunction because it leads to an analytical solution. We derive this full analytical solution in Appendix 2.D. We are only interested in the stationary limit, which we obtain by taking $\kappa \to \infty$. In this limit, the expression for routing efficiency is identical to the one obtained for maximally entangled states generated with a three level atomic cascade [28]. Maximizing this expression with respect to the bandwidth δ with and without the linear optical unitary yields routing efficiencies of 90% and 77% respectively.

Our analysis for the input state given by eq. (2.13) suggests that a stationary time-energy correlated input $\xi s(|t_2 - t_1|)$ can significantly improve the routing efficiency over uncorrelated inputs. Stationary inputs with different pulse profiles could yield further improvements. In the previous section, uncorrelated inputs with a Gaussian pulse profile yielded a bigger maximum for routing efficiency than Exponential pulses. We therefore consider the following input state:

$$|\Psi_{\text{in}}\rangle = \int_{-L}^{L} \mathrm{d}t_1 \int_{t_1}^{\infty} \mathrm{d}t_2 \sqrt{\frac{\delta}{\pi L}} e^{-\frac{\delta}{2}(t_2-t_1)^2} \hat{a}^{\dagger}_{\text{in}}(t_1)\hat{a}^{\dagger}_{\text{in}}(t_2)\,|0\rangle \tag{2.14}$$

Note that this state corresponds to substituting a Gaussian $F(\omega) = e^{-\frac{2\omega_1^2}{\delta^2}}$ in eq. 11. Here, $\delta \geq 0$ gives the bandwidth of the Gaussian and hence, of the input pulse. We note that

in this case the stationary limit corresponds to L → ∞. For this input state, the routing efficiency is calculated via numerical integration.

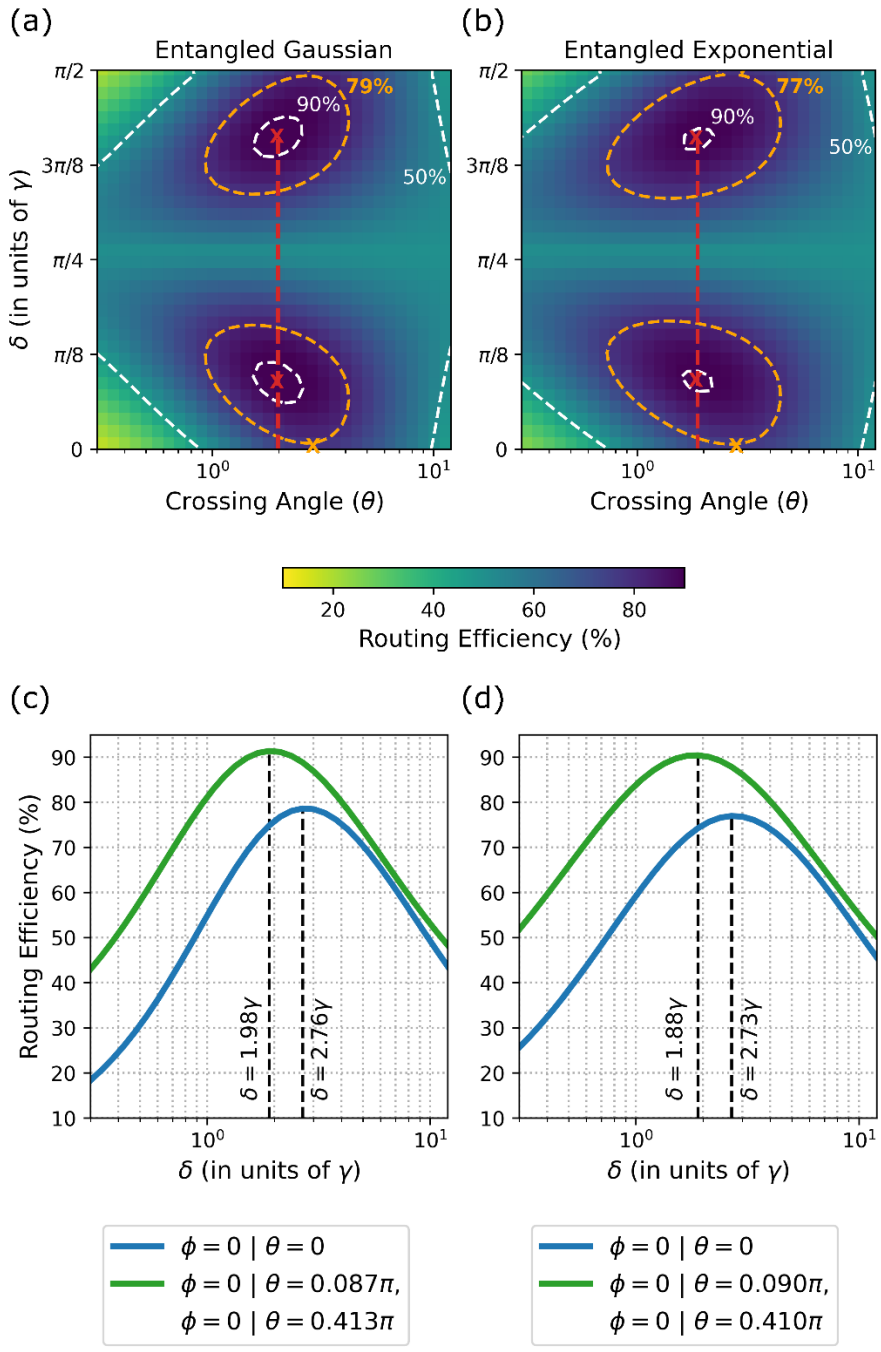

Figure 10 Routing efficiency for entangled inputs (see text for details)

Figures 10(a) and 10(b) plot the resulting routing efficiency as a function δ and θ for stationary entangled inputs with Gaussian and Exponential pulse profiles respectively. Since the routing efficiency is periodic in θ, we plot only one period. Each point on these plots corresponds to optimizing the routing efficiency with respect to ϕ. We obtain the same dependence on ϕ as for the uncorrelated inputs such the routing efficiency optimized for ϕ is mirrored across $\theta = \pi/4$. The red dots correspond to the routing efficiencies obtained by optimizing the linear optical unitary, which are 91.5% and 90% for entangled Gaussian and exponential pulses respectively. These lie within the orange contours that represent the blockade limited routing efficiencies. We note that the blockade limited routing efficiency of 77% corresponds to the value obtained in ref. [28] for input photons generated by a three-level atomic cascade.

We now compare the routing efficiency with obtained with the bare atom and the optimal linear optical unitary for both exponential and Gaussian entangled pulses. To make this comparison, we plot these two cases for Gaussian and exponential pulses in figures 10(c) and 10(d) respectively. The blue curves correspond to having no unitary on the outputs of the atom, and give the blockade limited efficiency. The green curves corresponds to the unitary transformations which optimize the routing efficiency. For the entangled exponential, the blockade limited efficiency of 77% occurs at the bandwidth $\delta = 2.73\gamma$. The bandwidth δ needs to be reduced to 1.88γ to obtain the maximum routing efficiency with the optimized linear optical unitary. For the Gaussian pulse, we also observe a reduction in the optimal bandwidth of the input pulse in going from the bare atom to adding the optimized linear optical unitary transformation after the atom. The optimal bandwidths in the two cases are 2.76γ and 1.98γ respectively.

Therefore, for entangled exponential and Gaussian inputs, the linear optical unitary changes the time-bandwidth tradeoff required to optimize the routing efficiency. This is in line with our findings for uncorrelated inputs in the previous section.

2.4 Pulse Optimization

In the previous section we assumed that the entangled photon wavefunction takes on the specific form of a Gaussian or exponential. In this section we employ optimization to obtain an optimal pulse shape that achieves the globally optimum routing efficiency. This optimal waveform represents a strong upper limit for the routing efficiency.

To optimize the entangled photon pulse shape, we expand the stationary wavefunction $\xi s(|t_2 - t_1|)$ in a complete expansion basis. We choose the Gauss-Hermite basis given by:

$$\xi_r(t) = \sum_{n=0}^{N/2} \alpha_n \mathrm{H}_{2n}(\delta t), \qquad \text{for even } N \tag{2.16}$$

where Hn(x) are the normalized Gauss-Hermite polynomials and N/2 gives the number of terms in the basis expansion. The terms αn are the coefficients of the respective polynomials, ensuring that the function ξs(t) is normalized. We choose the Gauss-Hermite basis because the first order term is a plain Gaussian. We have already analyzed this case in the previous section and found that it achieves 91.5% routing efficiency, which is close to unity. We therefore expect that higher order terms will add only small corrections, and we will only need to keep a few of them to come close to the global limit. Note that we keep only even terms in the sum in eq. (2.16), which corresponds to expanding ξ(t) over only the even Hermite-Gauss functions. We can

ignore the odd Hermite-Gauss functions without any loss of generality because $t \geq 0$, so we can express any function on the positive time axis using only even functions of time.

Since the scattering amplitudes ψ_{pq} and s_{lm} are linear in the input pulse, the output scattering amplitudes for the input pulse $\xi(\tau')$ denoted by $s_{pq}[\xi]$ can be written in general as:

$$s^{\mathrm{pq}}[\xi] = \sum_{n=0}^{N/2} \alpha_n s^{\mathrm{pq}}[H_{2n}] \tag{2.17}$$

The splitting efficiency is obtained by integrating $|s_{cd}|^2 + |s_{dc}|^2$ over the output photon creation times τ_1 and τ_2. For example, $\Gamma_{cd}[\xi] = |s_{cd}[\xi]|^2$ is given by:

$$\Gamma^{cd}[\xi] = \sum_{m=0}^{N/2} \sum_{n=0}^{N/2} \alpha_m^* \alpha_n s^{\mathrm{cd}}[H_{2m}] s^{\mathrm{dc}}[H_{2n}] \tag{2.18}$$

where we use the fact that the scattering amplitudes for real valued input states are real (see eqs. (2.10)). This can be rewritten as:

$$\Gamma^{cd}[\xi] = \alpha^\dagger \rho^{cd}[H] \alpha \tag{2.19}$$

where α is a column vector with entries α_1 thru $\alpha_{N/2}$ and ρ_{cd} is a symmetric matrix because $s_{cd}[H_{2m}]s_{dc}[H_{2n}] = s_{cd}[H_{2n}]s_{dc}[H_{2m}]$ implies that $\rho^{cd}_{ij} = \rho^{cd}_{ji}$.

Γ^{dc} takes a similar form and therefore the probability density $\rho_s[\xi]$ of the splitting the photons to output ports c and d takes a similar form.

$$\rho_s[\xi] = \alpha^\dagger \rho_s[H] \alpha \tag{2.20}$$

where the matrix $\rho_s[H]$ is a symmetric matrix. Integrating $\rho_s[\xi]$ over τ_1 and τ_2 is the same as integrating the entries of the matrix $\rho_s[H]$ over τ_1 and τ_2, which yields another symmetric matrix R. Note that the diagonal entries of R are simply the routing efficiencies for the different basis elements. Therefore, the splitting efficiency for the input state ξ can be written as:

$$P_S(\alpha) = \alpha^\dagger \mathrm{R} \alpha \tag{2.21}$$

Note that R is a symmetric positive semi-definite matrix because $P_S(\alpha) \geq 0$. We claim that the maximum $P_S(\alpha)$ is obtained for α_{max} which is the eigenvector of R corresponding to its maximum eigenvalue. To see this, we first diagonalize $R = U^T D U$ using the spectral theorem for symmetric matrices. Since, R is positive semi-definite, all entries of the diagonal matrix D are positive. The splitting efficiency can be rewritten as:

$$P_S(\beta) = \beta^\dagger \mathbb{D} \beta \tag{2.22}$$

where $\beta = U \alpha$ and the normalization constraint $\alpha^\dagger \alpha$ is equivalent to the constraint $\beta^\dagger \beta$. Therefore, $P_S(\beta)$ is clearly maximum when the vector β_{max} has zero valued entries everywhere except the position corresponding to the maximum diagonal entry of D, which is the maximum eigenvalue of R. The entry at this position can be chosen to be 1 because the overall phase of the input state doesn't matter. Therefore, the vector $\alpha_{max} = U\beta_{max}$ is the eigenvector of R with the maximum eigenvalue. To find the maximum routing efficiency, we construct the matrix R for different number of terms in the basis

expansion. The maximum eigenvalue of R then gives the maximum routing efficiency. Using the corresponding eigenvector α_{max} of R in (eq. 2.14) gives the optimal pulse shape in each case.

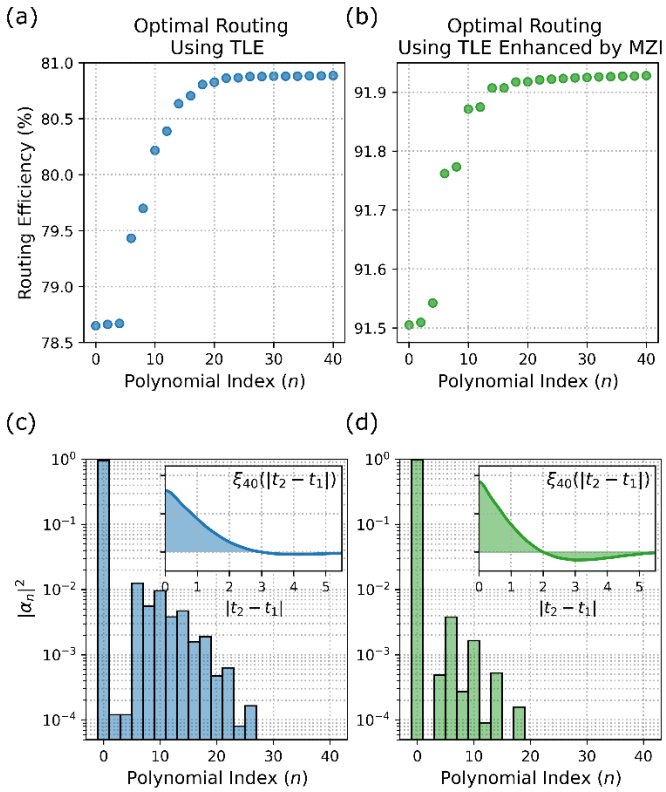

Figure 11 pulse optimization results (see text for details)

Figures 4(a) and 4(b) shows the dependence of the maximum routing efficiency on the highest order N of the Gauss-Hermite polynomial in the basis expansion of the input wavefunction. Fig 4(a) plots this for the case when the two-level emitter alone is the router. The maximum routing efficiency in this case is 81%. Fig 4(b) shows the case where the optimal linear optical unitary enhances the maximum routing efficiency to 92%. In both cases, when the input pulse is Gaussian, such that N=0, the routing efficiency is very close to the value it ultimately saturates to. This shows that the Gaussian pulse shape is very close to the optimal pulse shape of the input wave-

function. Figures 4(c) and 4(d) show the optimal pulse shapes corresponding to N=40 in figures 4(a) and 4(b) respectively. As expected, both these pulse shapes appear visually close to Gaussians.

2.5 Discussion and Conclusion

In conclusion, we have presented an extensive theoretical analysis of the splitting of two indistinguishable photons to spatially distinct output channels using a two-level emitter followed by a Mach-Zehnder interferometer. Through optimization of the input pulse shape and the phases of the interferometer, we obtain a routing efficiency of 92%. This is a substantial improvement over the optimal routing efficiency with just the two-level emitter, which is close to 81%. Our results exceed the maximum routing efficiency of 77% with a two-level emitter calculated in ref. [28]. Our results suggest that a stationary pulse can extract the optimal nonlinear response from the two-level atom. This insight could be applied to the optimization of other applications where the nonlinear response of a two-level is used. Throughout this work, the phases of the linear optical unitary were constant in time. We expect that the optimization of time-varying unitaries would further improve the splitting efficiency. We can also consider networks where multiple two-level emitters are cascaded with linear optical unitaries. Optimization of such networks may improve the fidelities of operations besides photon-photon splitting that we considered here.

Chapter 3: Diode Heterostructures for InAs/GaAs quantum dots

3.1 Introduction

We described the basic principle behind self-assembled quantum dots in chapter 1, section 1.3. Sticking with the example of InAs/GaAs quantum dots, we introduce here the idea and some of the existing literature on controlling the electrical environments that quantum dots are embedded in.

The semiconductor nature of quantum dots allows control of their electrical environment by making diode heterostructures. This locks the Fermi energy and provides electrical control of the quantum dot charged state. Layers of these heterostructures can be doped or undoped semiconductors and even metals, in the case of a Schottky diode heterostructure [111].

We are interested in controlling both the electrical and photonic environment of the dots. To make, for example photonic crystals, the basic building block is a thin GaAs membrane. Charge control on quantum dots in photonic crystals has been demonstrated using thin p-i-n diode structures. However, the large in-built electric field in combination with the small thickness of these devices led to a large potential at the position of the quantum dots shifting the Coulomb plateaus to large forward bias voltages. This resulted in high tunneling currents at the operating bias in p-i-n-membrane devices, a possible explanation for the absence of spin pumping in embedded quantum dots [119]. The quantum dot optical linewidths were relatively high in these structures.

In the second section of this chapter, we introduce p-i-n-i-n diode heterostructures, which we use for experiments throughout this thesis. These structures solve the problem of high currents that p-i-n diodes suffer from[111]. In the third section, we describe our results on noise spectroscopy of quantum dot electron spin embedded in a p-i-n-i-n diode.

3.2 p-i-n-i-n diode heterostructure

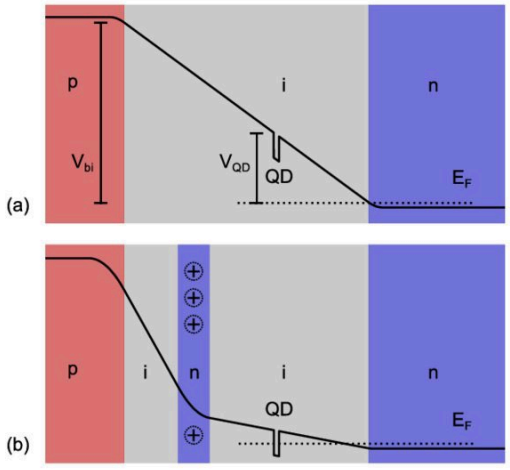

Figure 12 pin and pinin diode band diagram

Figure 12(a) shows a schematic of the p-i-n diode heterostructure along with the conduction band profile as a function of position under zero forward bias. We see that in order to bring the potential in the quantum dot beneath the E_F of the back n-contact, we have to apply a forward bias of V_{QD}. This leads to high currents flowing through the device when there is an electron in the dot, which is undesirable.

Fig 12 illustrates how a p-i-n-i-n structure solves the problem of high currents present in p-i-n structures when deterministically charging the dot with one electron. This is

achieved by adding a highly doped n layer to cause band bending, such the dot potential is very close to E_f even under no forward bias. This means that we need to apply a very small forward bias to charge the dot with one electron.

Loebl et. al. first demonstrated optical spin pumping of negatively charged quantum dots in p-i-n-i-n diode heterostructures in 2017 [111]. Interfacing of dots in these structures to photonic crystals by Zhouchen et. al. showed a record high cooperativity of 13 [100]. These results show that p-i-n-i-n diode heterostructures are a promising route towards realizing high quality spin-photon interfaces with semiconductor quantum dots.

3.3 Noise spectroscopy via dynamical decoupling pulse sequences

3.3.1 Level structure of negatively charged dots under Voigt magnetic field

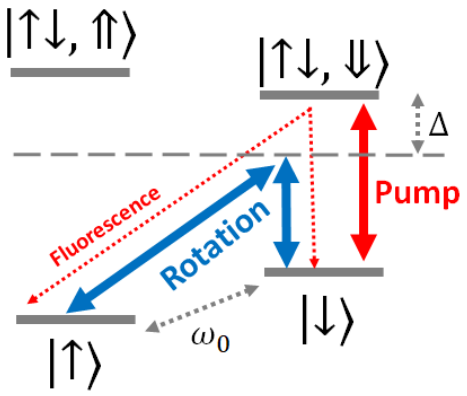

Figure 13 Level structure of negatively charged dot under voigt magnetic field

Fig 13 shows the level structure of a negatively charged quantum dot when a magnetic field is applied in the plane of the quantum dots i.e., perpendicular to the quantum dot

growth direction. This magnetic field direction corresponds to the Voigt configuration. The two ground states with spins up and down come from the spin states of the trapped electron which makes the dot negatively charged. In order to coherently control the spin state of the electron over the Bloch sphere, we need initialization of the spin to one of the spin states. The figure 13 shows how an optical pump can initialize the spin to the $|\uparrow\rangle$ state. After initialization to this state, we can rotate the spin state around the x or y axes of the Bloch sphere using a two-photon drive in the adiabatic limit. We describe in the next section how this drive is realized experimentally. Rotation of the spin around the z-axis of the Bloch sphere, which is defined by the direction of the applied magnetic field, is achieved by the free precession of the spin around the applied magnetic field. Note that ω_0 denotes the Zeeman splitting of the electron spin under an applied magnetic field. For comprehensive information about the spectrum of InAs/GaAs quantum dots under different conditions, we refer the reader to the spectroscopy and analyses performed by Bayer et. al. [49]

3.3.2 Experimental realization of rotation drive for electron spin

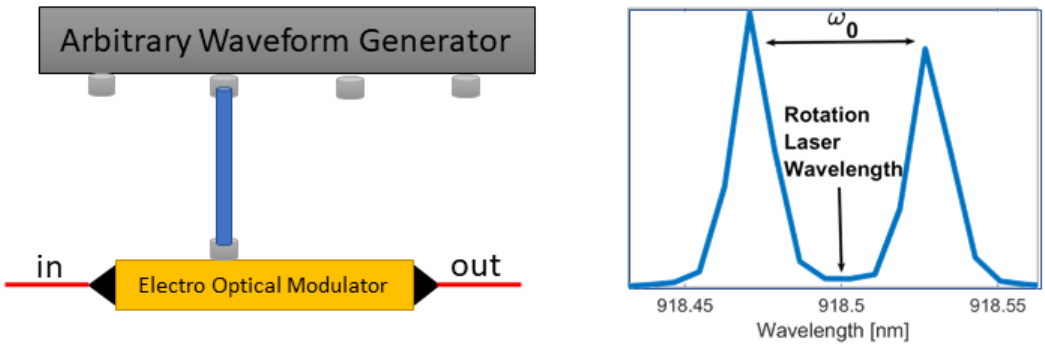

Figure 14 modulating a CW laser for creating rotation pulses

Figure 14 shows a schematic of how we realize the optical pulses that drive the electron spin and a spectrum of the realized optical pulses. An electro optical modulator from IX Blue (bandwidth >20 GHz) amplitude modulates a CW laser with linear polarization. The modulation signal is generated with a 65 GHz Arbitrary Waveform Generator. The Rotation wavelength is red detuned by Δ from the $|\downarrow\rangle$ to $|\uparrow\downarrow, \Downarrow\rangle$ optical transition. We apply a modulation signal with frequency $\frac{\omega_0}{2}$, where ω_0 is the Zeeman splitting between the optical transitions. The amplitude modulated signal then has two sidebands separated by ω_0, as shown by the spectrum in figure 14. By switching the modulation signal on and off, we can create pulse sequences that create the desired drive for the electron spin. As mentioned in the previous subsection, this external drive combined with the free precession of the electron spin around the applied magnetic field enables full SU (2) control (i.e., over the entire Bloch sphere) of the spin state [59].

3.3.3 Dynamical Decoupling Pulse Sequences

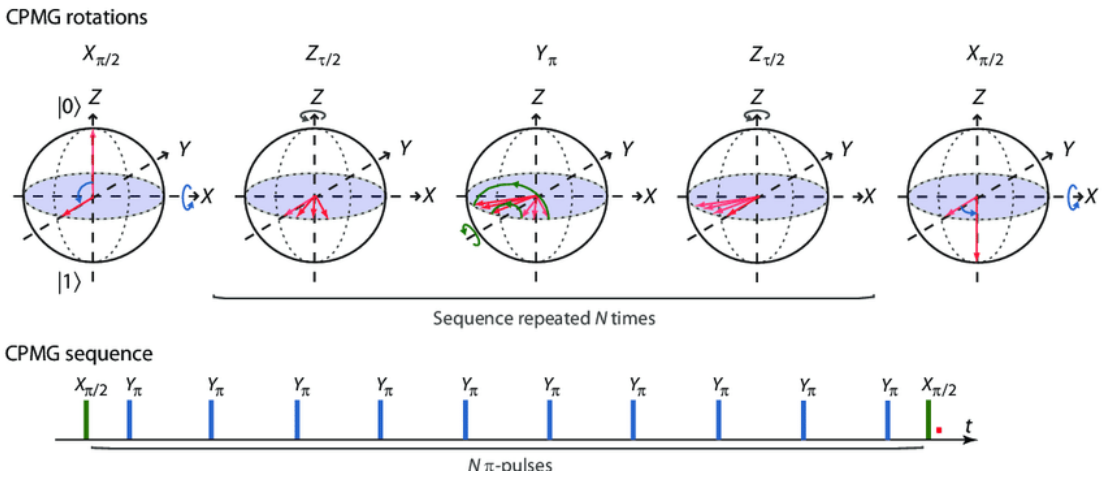

Figure 15 Dynamical decoupling to preserve spin coherence

Figure 15 illustrates the idea behind dynamical decoupling pulse sequences via the example of Carr-Purcell-Meiboom-Gill sequences [41]. We assume that the two-level system being interrogated is the spin ½ of the electron and the main decoherence mechanism is its interaction with the nuclei of the host lattice. We use a Bloch sphere representation of spin dynamics. Without loss of generality, we may assume that spin $|\uparrow\rangle$ state corresponds to the $|0\rangle$ state of a qubit and the spin $|\downarrow\rangle$ state corresponds to the $|1\rangle$ state.

The initial state of the spin is $|0\rangle$. We apply a $\frac{\pi}{2}$ pulse about axis such that the red arrow in the figure lands on the x-y plane, as shown by the first Bloch sphere in the figure (from the left). The second Bloch sphere in the figure shows multiple red arrows for the spin state after its free precession about the z-axis. This is to illustrate the decoherence of the spin dynamics due to its interaction with the nuclei and the multiple red arrows represent a lack of knowledge of the spin state of the electron. The third Bloch sphere shows the application of a π pulse about the y axis. After the application of the π pulse, the spin "rephases". This is illustrated by the red arrows coming together during the free precession following the π pulse.

Depending on how fast the interaction between the nuclei and electron spin is, we must apply multiple π pulses with separation smaller than the time scale of the interaction. One of the sequences of multiple π pulses is the CPMG sequences, which is shown in the figure.

3.3.4 Noise spectroscopy of electron spin in InAs/GaAs quantum dot

The interaction between the nuclei and the electron spin can be seen as causing noise in the electron spin dynamics [41-46]. By applying dynamical decoupling pulses in the CPMG sequence, with different number of pulses and with different time delays between pulses, we can extract the spectrum of this noise that affects the spin dynamics[41].

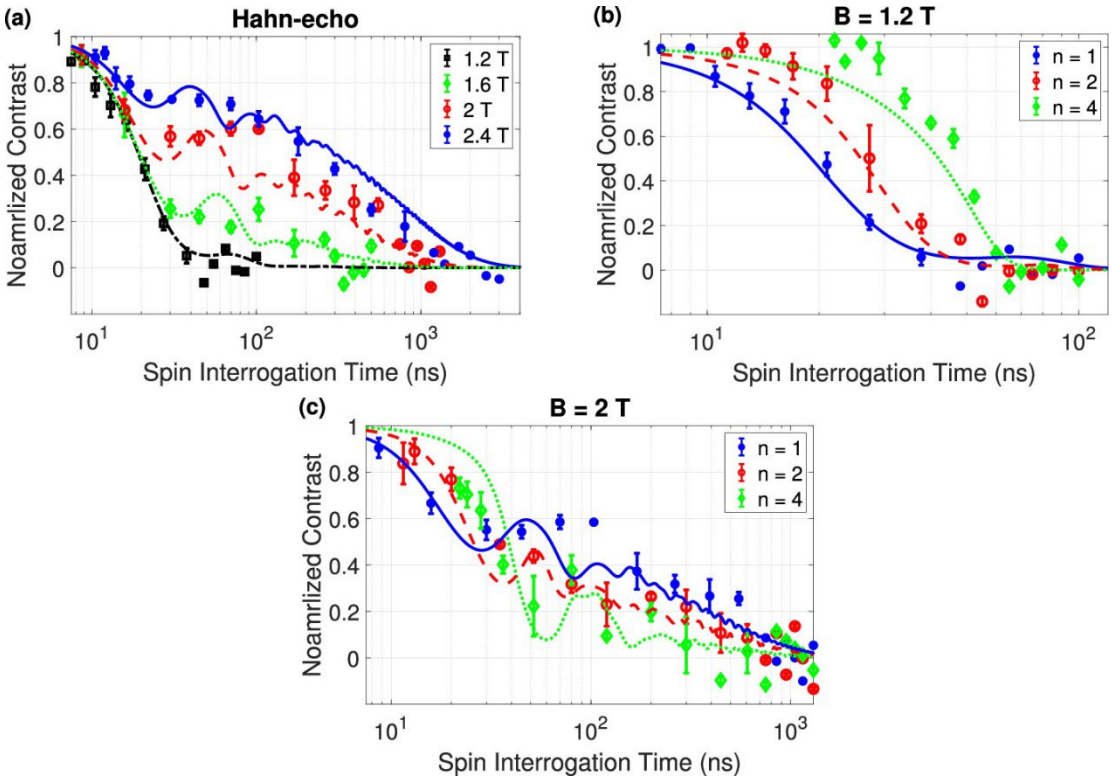

Figure 16 Resulting spin coherence curves from dynamical decoupling pulse sequences

We first apply the simplest form of the CPMG sequence: namely, the Hahn-echo experiment consisting of a single π pulse (Figure 16a). Consistent with previous Hahn-echo measurements on quantum dots, [57,71,72] the decay time scale of the spin dynamics (i.e., the coherence time) increases as a function of the external magnetic field, B, up to T2 ≈ 1 μs (blue dots in Figure 16a). This increase is associated with the Zeeman terms of the indium and arsenic nuclei dominating over the inhomogeneous

broadening of these nuclei at high magnetic fields (Supporting Information). Furthermore, the spin exhibits a two-stage decay in its coherence that consists of a fast drop of the signal contrast (at $T \approx 30$ ns), followed by a second decay (starting at $T \approx 100$ ns). This behavior is analogous to previously observed Hahn-echo spin dynamics of quantum dots.[57,72] Intuitively, the two stages of decoherence suggest that separate spectral components of the noise affect the spin dynamics at separate time scales. Simulation results (the lines in Figure 16a), which consider such separate noise components associated with the strained nuclear environment of the quantum dot [56,57], agree with the experimental results, thereby confirming this hypothesis. To experimentally extract these spectral noise components, we apply CPMG sequences with increasing numbers of pulses.

The temporal dynamics of the quantum dot spin under the application of such sequences are presented in Figure 16 b,c for the external magnetic fields of 1.2 and 2 T, respectively. As shown in Figure 16b for $B = 1.2$ T, the measured spin coherence times increase with n as the decay time scale of the coherence function becomes longer. However, as shown in Figure 16c, the two-stage spin decoherence profile for $B = 2$ T exhibits a more complicated behavior as a function of n. Our simulations (the lines in Figure 16 b,c) considering two spectral components of the Overhauser field [56,57] agree with the observed experimental behavior. However, to understand these complex dynamics requires a comparison between the rate of application of these pulses with the frequencies of the noise spectra. [41,43−46,57,73−75]

We experimentally extract these noise frequencies by analyzing all data collected from four different measurements of the coherence functions under the application of CPMG sequences with n = 1, 2, 4, and 8 π-pulses utilizing a recursive numerical integration method. The extracted spectral densities, plotted for external magnetic fields between 1.2 and 2 T (blue dots in Figure 17a–c), display a broad range of frequencies of up to 100 MHz. To characterize the behavior of the noise as a function of the magnetic field, we fit the extracted spectra to Gaussian functions (solid blue lines in Figure 17a–c). The central frequency of the noise (center of the Gaussian fit) increases with the magnetic field up to 38 MHz at B = 2 T (Figure 17d), corresponding to (twice) the Larmor frequency of indium nuclei [58] that dominate the interaction with the electron spin due to their spin-9/2 nature. Meanwhile, the amplitude of the noise (at the central frequency) decreases with the magnetic field (Figure 17e) as nuclear Zeeman interactions dominate over the broadening of the nuclei due to strain fields. [56,57]

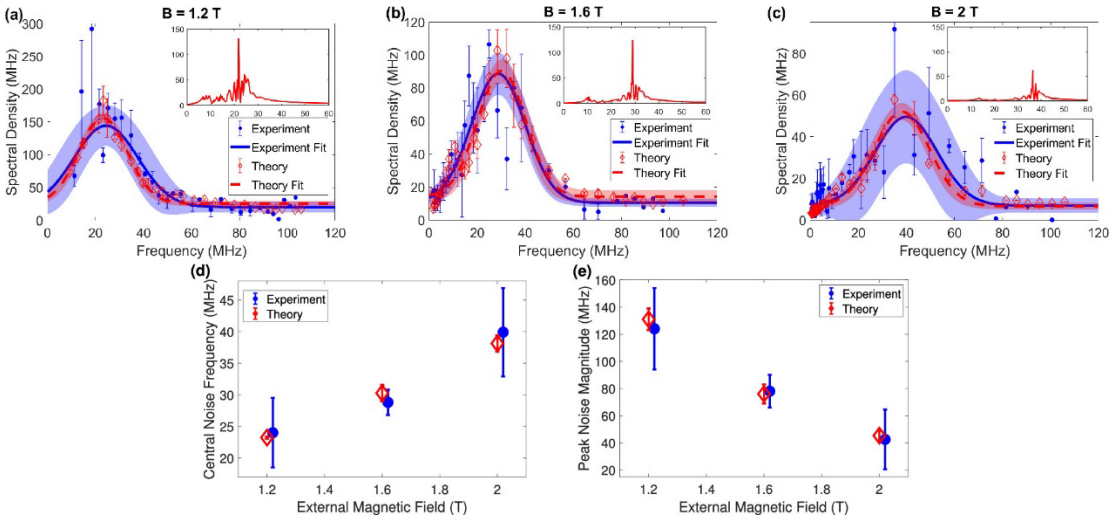

Figure 17 Extracted noise spectra (see text for details)

The extracted noise spectra verify a previously established theoretical model of the Overhauser field [56,57]. Using this model, we simulate the noise spectra that represent the hyperfine coupling of the quantum dot spin to indium and arsenic nuclear spins experiencing quadrupolar coupling to strain fields (insets of Figure 17a–c), which exhibit sharp peaks that correspond to the different nuclear spin numbers. To compare the experimental results of noise spectroscopy with theory, we first use the theoretical spectra to calculate CPMG coherence functions with n = 1, 2, 4, and 8 π-pulses under ideal conditions. We then apply the algorithm used to extract noise spectra from the experimentally obtained coherence functions to the simulated coherence functions (red diamonds in Figure 17a–c). As the CPMG sequences probe the noise with spectrally broad filter functions that have high harmonics rather than with delta-like filter functions that probe the noise at single frequencies, the sharp peaks in the simulated spectra are broadened by the finite sampling resolution and can be fitted to Gaussian functions similarly to the experimental results. The dashed red lines in Figure 17a–c that represent such Gaussian fits lie well within the uncertainties of the experimentally fitted results (shaded blue areas), thereby confirming the agreement between theory and experiment. Furthermore, the amplitudes of the simulated spectra (red diamonds in Figure 17e) consistently fit the experimentally extracted amplitudes and indicate that the quantum dot spin interacts with 40000 nuclei, in agreement with common predictions. [57]

The theoretical model of the quantum dot environment verified by all-optical noise spectroscopy can shed light on the coherent behavior of the quantum dot spin dynamics

(e.g., the coherence functions in Figure 16). The model predicts two separate noise terms, perpendicular and parallel to the external magnetic field. [56,57] The noise component perpendicular to the external field, $S_{\perp}(\omega)$, monotonically decreases with the frequency and qualitatively fits the experimentally extracted noise floor (i.e., the baselines of the Gaussian fits in Figure 17a–c). This noise component dominates at low frequencies, thereby leading to the spin dynamics at long time scales (>100 ns) depicted in Figure 16. Since the application rate of π-pulses in our CPMG sequences is faster than the low frequencies of $S_{\perp}(\omega)$, increasing the number of pulses slows down the decay of the spin dynamics at long time scales. For example, under an external field of 2 T (Figure 16c), the decay of the spin dynamics at $T > 100$ ns is slower for $n = 4$ (dotted green line) than for $n = 1$ (solid blue line). In addition to the perpendicular noise term, the theoretical model predicts high-frequency noise, $S_{\parallel}(\omega)$, which arises in parallel to the direction of the external field. [56,57] This parallel term is stronger than the perpendicular term and consists of peaks corresponding to the nuclear Larmor frequencies broadened by the environmental strain field . The broad spectral features of $S_{\parallel}(\omega)$ lead to the observed contrast drop [75] at the short time scales depicted in Figure 16. For an external magnetic field of $B = 1.2$ T, the large magnitude of $S_{\parallel}(\omega)$ leads to the complete loss of the quantum dot spin coherence under the Hahn-echo sequence (dash-dotted black line in Figure 16a) at $T \approx 30$ ns; thus, a second decay caused by $S_{\perp}(\omega)$ is not observed for this field. The contrast drop caused by $S_{\parallel}(\omega)$ also quantifies the ability of the CPMG sequences to extend the quantum dot spin coherence time. For example, the application rate of the π-pulses in our CPMG sequences is slower than the high-frequency components of $S_{\parallel}(\omega)$ for $B = 2$ T. As a result, the decay

of the spin dynamics at time scales shorter than 100 ns does not improve by increasing the number of pulses (Figure 16c). By analyzing the obtained noise spectra, we learn that mitigating such high-frequency noise to extend the quantum dot spin coherence time from the current state of the art of a few microseconds [57,71,72] to beyond 10 μs requires the application of dynamic decoupling sequences utilizing hundreds of π-pulses.

However, here we can apply just eight π-pulses due to two mechanisms of spin relaxation. First, the natural spin relaxation of the quantum dot in our sample, $T_1 \approx 1$ μs, did not allow us to observe the expected spin dynamics under multipulse sequences beyond microsecond time scales. This relaxation time could be extended up to milliseconds by modifying the tunnel barrier of the sample. [76] Second, increasing the number of CPMG pulses in our measurements resulted in a dramatic contrast drop of the collected fluorescence as a function of n [60]. This contrast drop is related to electron tunneling due to the increase in the laser power associated with the addition of the pulses. Such electron tunneling could be mitigated by coupling the quantum dot to fabricated photonic structures that reduce the laser power required for spin rotation. The reduction of the rotation laser power could enable the realization of multipulse sequences for prolonging spin coherence times and for the preservation of arbitrary spin states (e.g., XY8-based sequences [73]) for quantum information processing. Furthermore, the implementation of multipulse sequences with ultrahigh spectral resolutions (e.g., the "DYSCO" sequence [44]) may enable the identification of individual Larmor frequencies associated with nuclear species (e.g., the peaks in the

insets of Figure 17), as well as the ultrahigh resolution probing of external fluctuating magnetic fields with a single spin.

Chapter 4: Large Purcell Enhancement and Dipole Induced Transparency in a Bullseye Cavity

4.1 Introduction

In recent years, optically active quantum dots have emerged as useful resources for photonic quantum technologies. Quantum dots emit single photons with high brightness and indistinguishability,[77−85] which makes them promising as sources of single and entangled photons for photonic quantum computing.[86−89] In addition, these dots can be electrically charged with a single electron or a single hole, thereby offering a ground-state spin qubit.[90−96] Strongly coupling a quantum dot spin to a photonic cavity could provide an interface between a single photon and a single spin for quantum information processing,[97,98] thereby contributing to the ongoing efforts of establishing quantum networks.[99,100] Such strong coupling requires a sufficiently high cooperativity between the spin and the cavity, which typically involves the use of high-Q (>10k) cavities.[97,98] An ultrahigh cooperativity has been recently achieved between a quantum dot and a high-Q tunable microcavity formed by utilizing the advanced fabrication of convex mirrors.[98] An alternative approach for achieving such high cooperativities utilizes simple nanofabrication tools (e.g., electron beam lithography) to fabricate photonic crystal cavities. However, high-Q photonic crystal cavities often feature poor optical access to external light from the free space due to their divergent far-field emission patterns. [92,97,101] This poor access limits the ability to optically excite and collect photons emitted from quantum dots, as well as to coherently control the quantum dot spin, which requires circularly polarized light.[91, 92, 95, 96].

To efficiently interface quantum dots with light often involves their coupling to low-Q (<1000) cavities such as gratings and micropillars.[80-82,84,102−107] Low-Q cavities can increase the optical density of states in the environment of a quantum dot, thereby Purcell-enhancing the rate of spontaneous emission of single photons from the dot. In addition, cavities that provide Gaussian far-field emission patterns can improve the efficiency of exciting and collecting photons from the quantum dot via confocal optical setups. For example, circular gratings formed by the periodical etching of rings from a substrate material (”bullseye” cavities) have been used to optically interface single defects in diamond [109] and quantum dots.[84,102,104−107,110] In particular, InAs/GaAs quantum dots produced optical emission of single photons with lifetimes of ∼200 ns.[106] Improving the efficiency of collecting photons from quantum dots coupled to such low-Q cavities can be achieved by introducing ellipticity to the structure,[84,85] but this prevents the access to the cavity using circularly polarized light. Another downside of low-Q cavities is their high loss of photons, which may result in low spin-cavity cooperativities, thereby significantly limiting the performance of the cavities for quantum networking. [97,98] To date, a low-Q cavity that provides a high-cooperativity spin−photon interface with an efficient, polarization-independent, optical access has yet to be demonstrated.

In this chapter, we efficiently couple InAs/GaAs quantum dots embedded in a charge-tunable device (a p−i−n−i−n diode) [101,111,112] to low-Q (∼1000) bullseye cavities with nearly degenerate polarization modes. By leveraging the low charge noise associated with the device, we measure spontaneous emission lifetimes of quantum

dots as short as ~80 ps (a Purcell enhancement of ~15), which are more than 2 times shorter than those previously observed for InAs/GaAs quantum dots in nearly degenerate bullseye cavities [106] and are close to the state-of-the-art lifetimes of such dots in microcavities.[80,81,84,85] By measuring a dip in the reflected light from a bullseye cavity caused by its coupling to an uncharged quantum dot, we extract a cooperativity of ~8 between the cavity and the dot, which highlights the potential of the bullseye cavities as spin−photon interfaces. Combined with the enhanced efficiencies of optically exciting the quantum dot spin and collecting the emitted photons, the fabricated bullseye cavities offer a promising platform for quantum information processing utilizing electrically charged quantum dots.

4.2 Relevant Theory: Purcell Enhancement

Purcell enhancement is one of the phenomena in quantum optics that needs the quantization of electromagnetic radiation for a complete description. This is because Purcell enhancement is concerned with the enhancement of the rate of spontaneous emission of an electric dipole (i.e., atom which interacts with the electromagnetic field with the electric dipole Hamiltonian $\hat{d}.\hat{E}$) when it is coupled to a single mode of electromagnetic radiation in the weak coupling regime of cavity QED.

A two-level atom (with an electric dipole) spontaneously emits radiation even in the absence of any externally applied field because of its interaction with the vacuum modes of electromagnetic radiation. When the atom is coupled to a cavity which supports only a single mode of the electromagnetic field, it sees a different electromagnetic environment than it sees when places in vacuo. This change in

electromagnetic environment then changes the rate of spontaneous emission of the atom.

When the atom is in resonance with the mode of the optical cavity, the rate of its spontaneous emission becomes faster than its rate in vacuum. The ratio of the rate in cavity to the rate in vacuum is known as Purcell Enhancement. Purcell Enhancement is given by:

$$F_p = \frac{3}{4\pi^2}\left(\frac{\lambda_{free}}{n}\right)^3\left(\frac{Q}{V}\right)$$

where λ_{free} is the vacuum wavelength, n is the refractive index, and Q and V are the cavity quality factor and the mode volume respectively.

In this chapter, we will demonstrate Purcell Enhancement of the InAs quantum dot excitons in a Bullseye cavity.

4.3 Relevant Theory: Dipole Induced Transparency (DIT)

Dipole Induced Transparency refers to the modification of the cavity transmission and reflection in the weak coupling regime of cavity QED i.e., when $g < \kappa$ and $g \gg \gamma$ (where g, κ and γ are defined in figure 1,) such that the cooperativity $C = \frac{g^2}{\kappa\gamma} > 1$. This regime is also known as the Purcell Enhancement regime. In this regime, the cavity transmission of the cavity with two symmetric mirrors as shown in figure 1 gets modified from a Lorentzian spectrum for the bare cavity to the spectrum shown in figure 18 which exhibits a dip at the resonance wavelength of the atom [113].

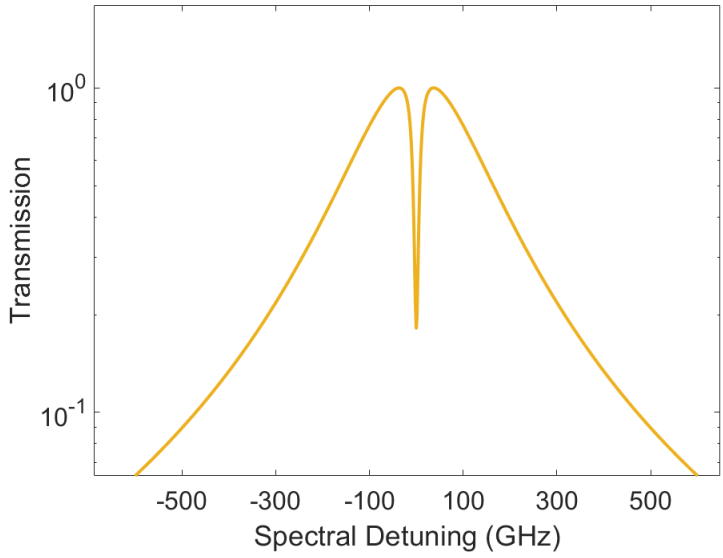

Figure 18 DIT: dip in cavity transmission at atomic resonance frequency

4.4 Design and simulation of Circular Bragg Grating (Bullseye) cavities

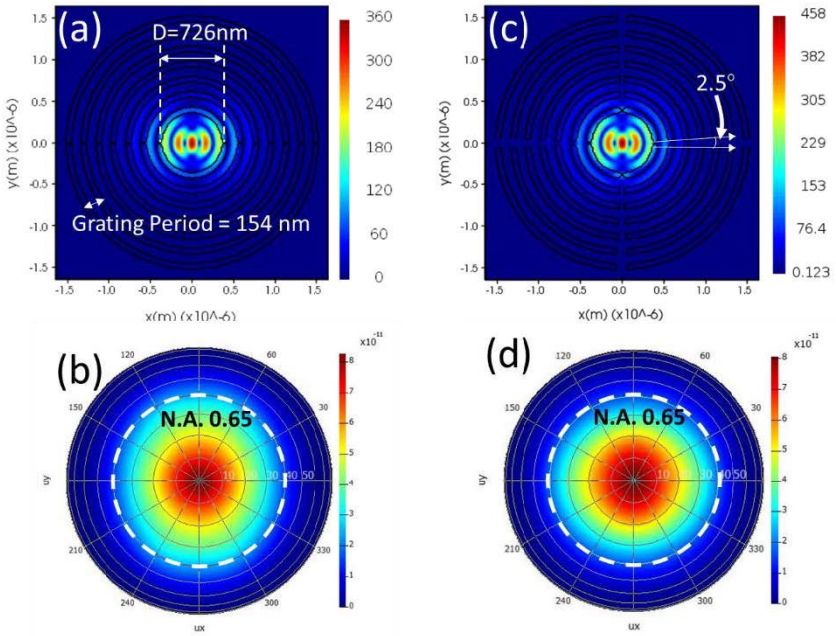

Figure 19 Bullseye design and simulation

Figure 19 shows the design, modal pattern and far field emission pattern of a circular Bragg grating aka Bullseye cavity. We designed and simulated the Bullseye cavities

using Finite Difference Time Domain (FDTD) simulation of Maxwell's equations using Lumerical. Figure 19 (a) shows the design parameters for a Bullseye cavity designed to have an optical mode at 930nm, which corresponds to the resonance wavelength of the majority of the InAs quantum dots in our wafers [101]. The bullseye cavity mainly is composed of two parts. One is the center disk that determines the resonance wavelength of its fundamental mode. For InAs quantum dots eimtting at around 930 nm, we set the radius of the center disk to be 363 nm to target a resonance wavelength of 930 nm. The second part is the surround ring gratings that help shape the Gaussian far field pattern (Figure 19 (b)), which is related to the radius of center disk and was set to be 154 nm here. To support the grating structure on a suspended GaAs membrane, we added bridges between the gratings to connect them to the bulk region as shown in Figure 19(c). To minimize the perturbation brought by those extra supporting bridges, we tried to minimize the size of those supporting bridges but made them wide enough to support the weight of the gratings. As shown in Figure 19(c), bridges of 2.5 degrees arc with respect to the center of the cavity were used. Figure 19 (c) and (d) are the y-dipole electrical field intensity and far field pattern of the bullseye cavity with supporting bridges. Compared to the simulation results of the original bullseye design in (a) and (b), introducing bridge structures doesn't affect the optical modes of bullseye cavity much. The simulation shows bullseye cavity typically features a quality factor of around 1000.

4.5 Fabrication steps for Bullseye Cavities

In this chapter, we demonstrate Purcell Enhancement of InAs quantum dot excitons embedded in pinin diode heterostructures using Bullseye cavities. We also show the Dipole Induced Transparency effect of the weak coupling regime of cavity QED.

Before we describe the measurement of our dot-cavity devices, we briefly describe the steps involved in the fabrication of Bullseye cavities. A detailed description of these steps can be found in ref. [121].

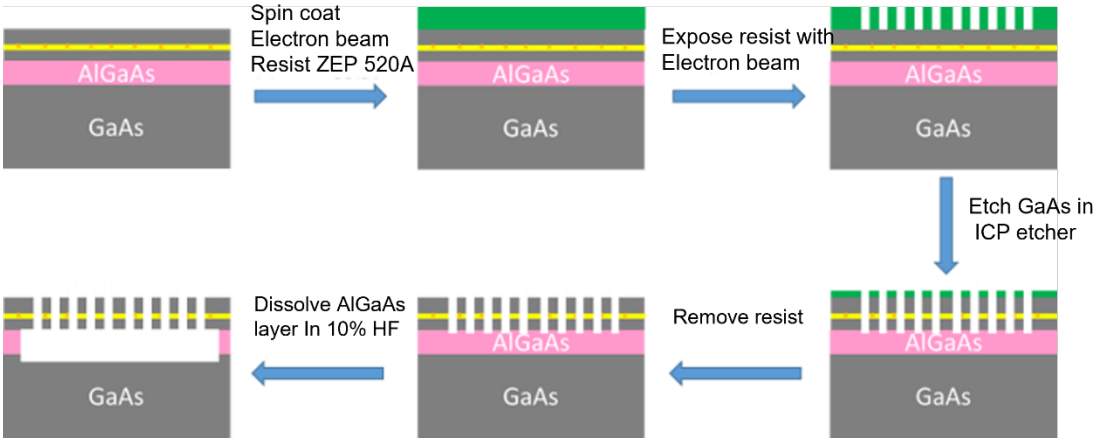

Figure 20 GaAs softmask fabrication steps

Figure 20 shows a schematic of the fabrication steps. First, we spin coat our quantum dot wafer with the positive electron beam resist ZEP520A (Zeon Chemicals) at a spin rate of 3000 rotations per minute. This leads to a resist thickness of ~450nm. We then expose ZEP520A with an electron beam lithography tool Elionix ELS G-100 which generates 100kV electrons. We use an electron beam current of 100pA to expose the resist. We dip the sample in a beaker containing ZED-N50 for 60 seconds to "develop" the resist. The exposed part of the positive resist dissolves in n-amyl acetate (sold as

ZED-N50 by Zeon chemicals.) This is followed the etching of GaAs in a Chlorine plasma. The resist of thickness ~450nm holds well under the chlorine plasma, allowing us to obtain the desired structures reliably. (We note that depending on the structures being fabrication, a "hard mask" of Silicon Nitride may need to used.) After etching, we remove the resist by dissolving it in n-methyl-2-pyrrolidone (sold as Remover PG by Kayaku chemicals.) The sample is kept in a remover PG beaker placed on a 60^{o}C hot plate for 20 minutes to completely remove the resist. To obtain suspended Bullseye structures, we dip the sample in 10% HF for 45 seconds. HF performs an undercut of the AlGaAs layer by producing AlH_3 which dissolves in water. However, it also leaves behind AlF_3 residues, which are removed by dipping the sample in KOH for 1 minute.

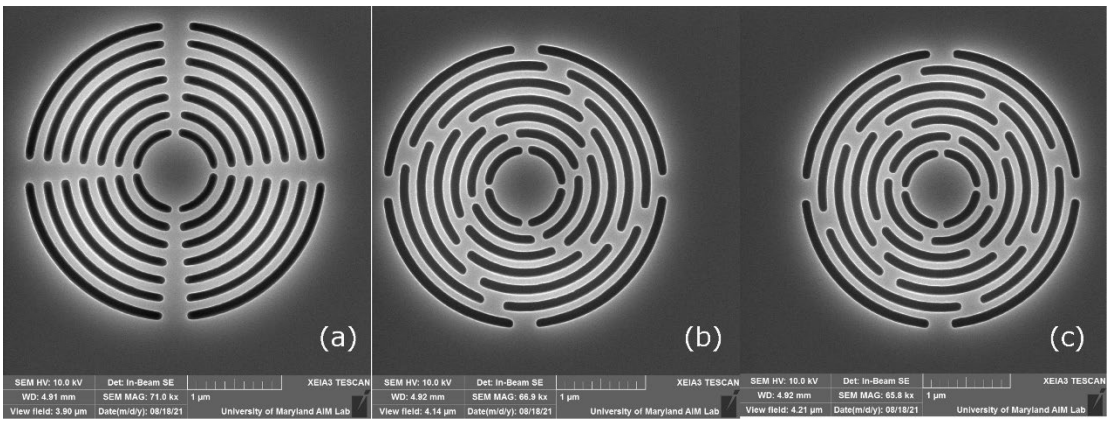

Figure 21 SEM images of fabricated bullseyes

Figure 21 shows all the three types of Bullseye structures we fabricate. As also mentioned in the previous section, we have bridges connecting subsequent rings of Bullseyes so that the structures don't collapse following their suspension due to undercut of the AlGaAs layer. The three structures shown here only differ in the

arrangement of these bridges and exhibit very similar far field emission patterns in simulation.

4.6 Characterization of Bullseye cavities

We first characterize the modes of the Bullseye cavities using above band photoluminescence measurements. It's possible to observe cavity spectra under photoluminescence due to the so-called cavity feeding effect[122.]To measure the bullseye spectra, we apply a voltage of 1V across the pinin diode. At this voltage, the lines in the spectra corresponding to emission from individual dots are strongly diminished, allowing an easy characterization of the locations and linewidths of the modes of the bullseye cavities.

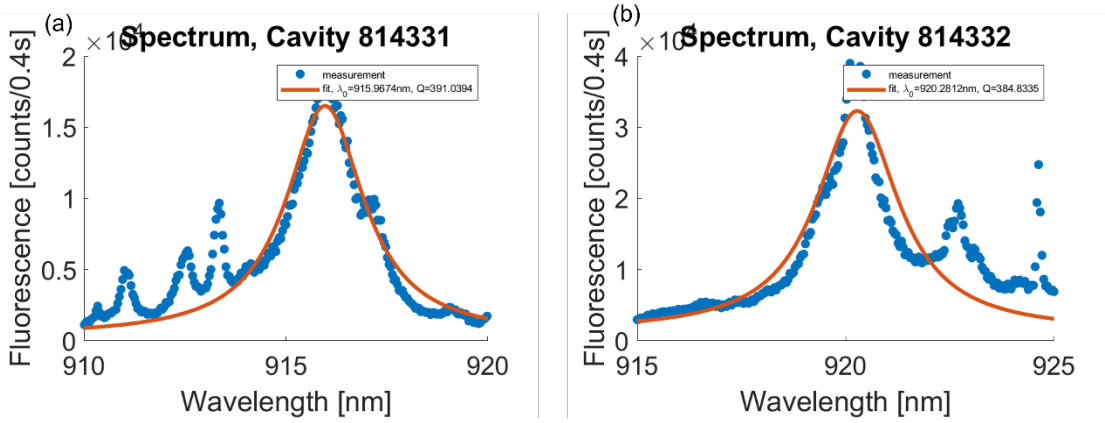

Figure 22 Bullseye photoluminescence spectrum

Figure 22 shows the two orthogonally polarized modes of a bullseye cavity that was ultimately deemed unsuitable for further cavity QED measurements. The label 8-14 33 identifies the location of this bullseye in the array of cavities that we fabricated. The last digits 1 and 2 in the labels in figure 22a and 22b respectively identity the two orthogonally polarized modes. This cavity was ultimately rejected for further measurements because of the low-quality factor (~400) of the two modes and the large

splitting of ~5nm between them. However, we performed time-resolved photoluminescence (PL) of the exciton coupled to the 814331 mode and compared with the same measurement of an dot exciton in the bulk i.e. a dot not physically located inside a bullseye cavity. These measurements are shown in Figure 23. We fit the observed PL to exponentials and extracted lifetimes of ~670ns and ~1400ns for the exciton coupled to the bullseye and the dot exciton in the bulk respectively. This corresponds to a Purcell enhancement of ~2, which further motivated us to keep looking for better devices in our array. Also note that the counts/unit time from the exciton in the bullseye are two orders of magnitude higher than the exciton in the bulk.

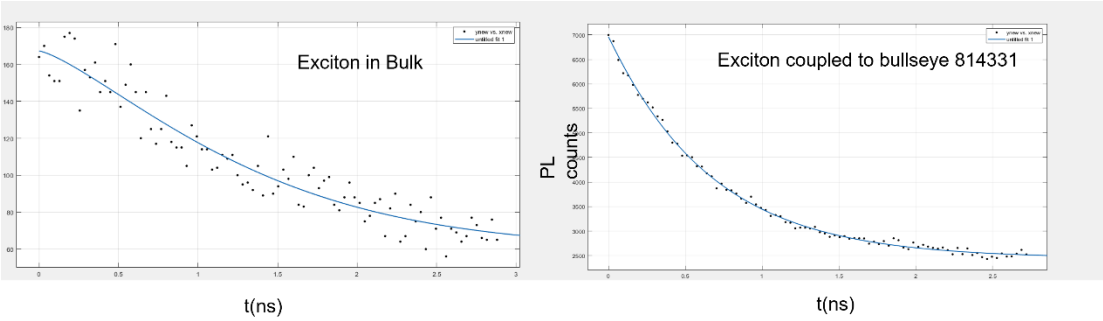

Figure 23 Exciton lifetime in bulk and bullseye

Figure 24 shows the above band PL measurements for the Bullseye labelled 8-14 11 which is the main focus of the rest of this chapter. Note that this bullseye has the bridge structure shown in figure 24(a). Figure 24(a) shows the PL spectrum at a bias voltage of 1V where only the cavity mode is observed. This Bullseye has nearly degenerate polarization modes. Furthermore, the modes have a Quality factor of ~1070 which agrees very well with the simulated quality factor. Figure 24 (b) overlays the PL from the two dots coupled to this bullseye measured at an applied magnetic field of 6T in the voigt configuration and a bias voltage of 0.6V where the two dots are neutral and show the brightest emission. At 6T, these neutral dots have two orthogonally polarized PL

lines, parallel and perpendicular to the applied magnetic field. For the rest of this chapter, we focus on Dot 1.

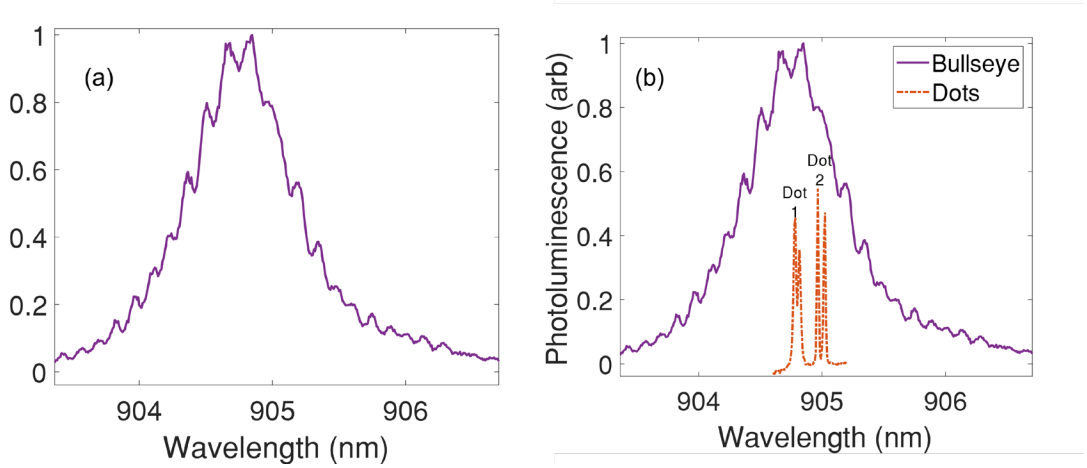

Figure 24 photoluminescence of (a) bullseye (b) of dots coupled to bullseye

4.7 Large Purcell Enhancement of a charge stabilized neutral dot in a Bullseye cavity

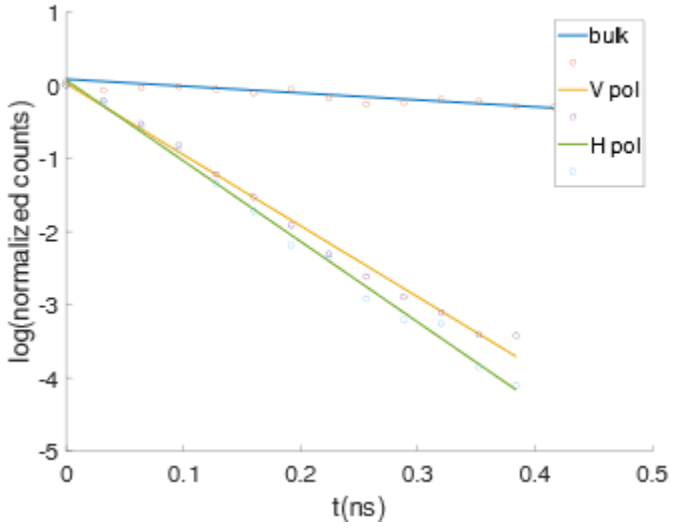

Figure 25 Lifetime measurements show large Purcell enhancement

Fig 25 shows the time-resolved photoluminescence measurements of the two orthogonally polarized transitions of dot 1 at 6T magnetic field in the voigt geometry and a representative measurement of a dot in the bulk. We plot the y-axis on a log scale such that the exponential decay of photoluminescence versus time is rendered linear on the plot. The blue, orange and green lines correspond to linear fits to the PL of bulk exciton, bullseye coupled V polarized exciton and H polarized exciton respectively. From the linear fits, we extract lifetimes of 83ps and 90ps for the H polarized and V polarized excitons respectively. In contrast, the lifetime of the bulk exciton is ~1200 ps. This suggesst a large Purcell enhancement due to the Bullseye cavity mode.

For the H polarized exciton, we calculated a Purcell enhancement of 15.35 ± 0.85. The latter is close to the state-of-the-art lifetimes measured on InAs/GaAs quantum dots embedded in microcavities [80,81,84,85] and is shorter by a factor of ∼2 than those previously measured on InAs/GaAs quantum dots in bullseye cavities with nearly degenerate polarization modes.[106] We attribute this improvement to two main factors. First, our fabrication of bullseye structures involves the etching of a sacrificial layer below the cavity, whereas the rings of the bullseye structures in previous fabrications [102,110] either were not etched all the way down to this layer or incorporated a metallic mirror at the bottom.[106] While partial etching or the addition of a metallic mirror could improve the collection efficiency of photons scattered from the sample, these procedures may reduce the quality factor of the bullseye cavity, thereby providing a smaller Purcell enhancement compared to those we observe for suspended structures. The second factor that contributes to the enhanced optical emission rate is the reduced charge noise associated with the p−i−n−i−n diode,

[101,112] which minimizes the effects of spectral wandering of quantum dots coupled to the cavity that may degrade the Purcell enhancement of their emission.

4.8 Bullseye cavities show dipole induced transparency.

To study the potential of bullseye cavities as spin−photon interfaces, we measure the reflectivity of light from a cavity coupled to an uncharged quantum dot in the absence of an external magnetic field. We sweep the frequency of a weak (∼0.5 nW) continuous-wave laser and measure the intensity of the signal reflected from the cavity (purple dots in Figure 26a). A dip in the cavity reflectivity with a contrast of ∼80% emerges at the wavelength of the optical transition of the quantum dot. This optical transparency is caused by the destructive interference between two optical transitions with opposite phases generated due to the coupling between the cavity and the quantum dot (in analogy with electromagnetically induced transparency where two transitions in an atomic three level system interfere destructively) and improves with the Purcell factor. [113] The observed reflectivity pattern is asymmetric, namely a Fano resonance,[114−116] possibly due to a small splitting between the cavity polarization modes or to an additional interference effect resulting from the membrane of our sample (see Appendix 3.A). The measured reflectivity agrees with simulation results based on a theoretical Jaynes−Cummings model [24,40] (yellow line in Figure 26a) considering a coupling strength of g = 35 GHz between the quantum dot and the cavity and photon losses from the cavity and the dot of κ = 310 GHz and γ = 1 GHz, respectively (see Section Appendix 3.A). The relatively high cooperativity between the

dot and the cavity extracted from the model, $C = \frac{g^2}{\kappa\gamma} = 4$, suggests that bullseye cavities can be used for photon switching and for interfacing single photons with single spins. [97,98]

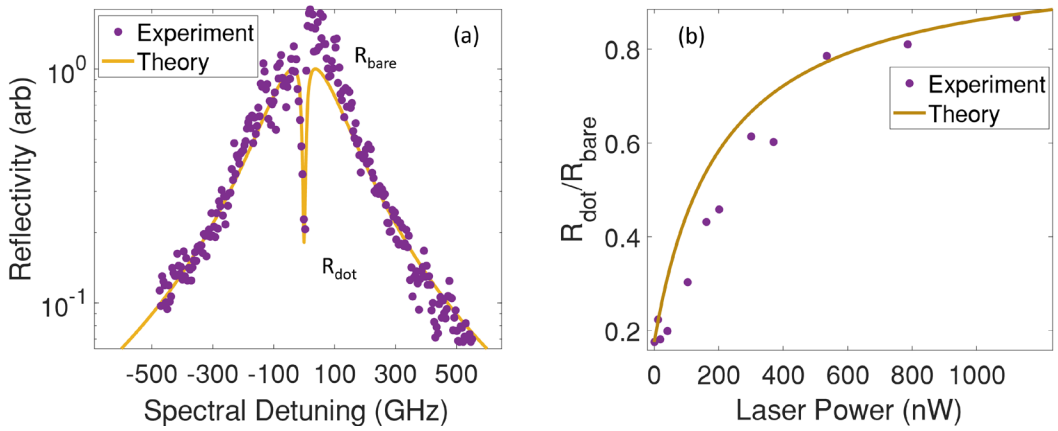

Figure 26 bullseye reflectivity measurements (see text for details)

We can estimate the efficiency of coupling photons to quantum dots in such interfaces by plotting the intensity of light reflected at the cavity dip as a function of the incident laser power (Figure 26b). Fitting the experimentally measured dip reflectivity trend to the theoretically simulated trend [40] reveals that ~8% of the incident light reaches the cavity (see Appendix 3.A). This efficiency is much greater than those we observe in the same experimental setup utilizing photonic crystal (e.g., L3) cavities, indicating that the far-field emission pattern of the bullseye cavity is concentrated at small angles, as expected from simulations. The main factor limiting the coupling efficiency is the mismatch between the numerical aperture of the objective lens in our setup (0.68) and the angle of the cavity far-field emission mode corresponding to a 1/e relative intensity (~0.36). This mismatch leads to a factor of ~3.6 degradation in the efficiency that can be avoided by changing the lenses in our experimental setup. After additionally

growing a distributed Bragg reflector at the bottom of the sample the sample to act as a mirror, we expect to optically access quantum dots in next-generation bullseye cavities with efficiencies of over 60%. Beyond improving the rates of optical excitation and photon collection, such efficient access of light may enable multipulse coherent control of quantum dot spins in cavities. [96]

4.9 Optical spin pumping in a Bullseye cavity

As we mentioned in chapter 1, in order to achieve perfect photon-photon entanglement, we require a lambda system with one of its transitions coupled to an optical cavity [99] To achieve this, we would like to use a negatively charged dot with magnetic field applied in the voigt configuration which has the desired level structure due to the metastable spin up and down states of the electron spin [93].

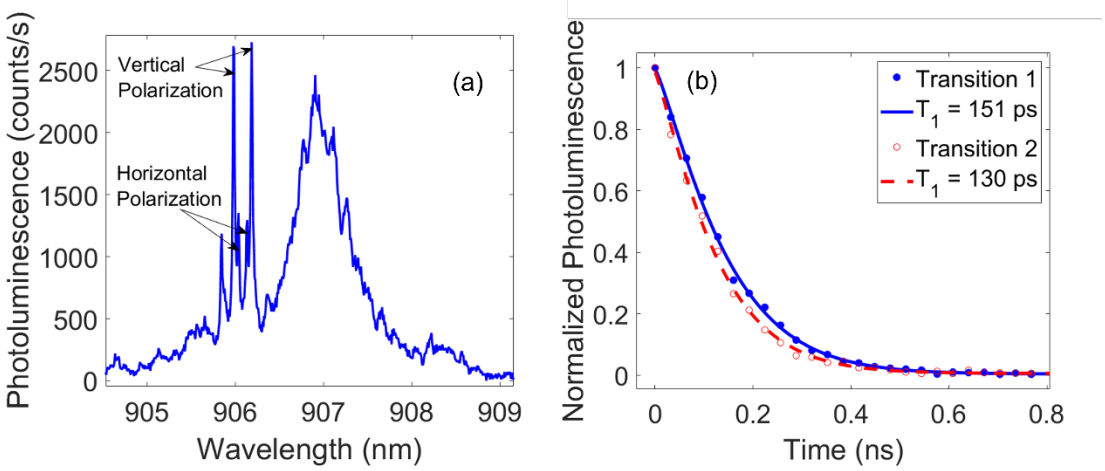

Figure 27 photoluminescence of bullseye coupled to charged dots (a) CW (b) time-resolved

We examine a bullseye cavity coupled to such a spin: namely, a single electron spin qubit confined in a ("charged") quantum dot. Under an external magnetic field of B = 9 T, the application of a series of ultrashort above-band laser pulses (i.e., they are much

shorter than the optical emission rates of the dot) reveals the optical transitions of the dot (Figure 27a). Compared to dots in the bulk, the laser power required for the saturation of the photoluminescence signal from the quantum dot in the cavity is 1 order of magnitude weaker, and the intensity of this signal is ∼25 stronger. Optically accessing the device should be even more efficient for light in spectral resonance with the cavity: namely, spectrally detuned by ∼1 nm from the optical transitions of the dot. Here, due to the observed spectral detuning, the Purcell enhancement of photon emission via the optical transitions of the examined electrically charged dot of (∼8−9, Figure **27**b) is smaller than that observed for the uncharged dot studied in the previous section. However, this spectral detuning can be leveraged to boost the efficiency of optical pulses that coherently control the quantum dot spin applied in resonance with the cavity, as such pulses must be spectrally detuned from the dot's optical transitions. [91,95,96] Another observation that highlights the potential of bullseye cavities for boosting spin-coherent control is the emission of photons from all four optical transitions of the dot. As illustrated in Figure 27a, the charged quantum dot emits photons at polarizations orthogonal to each other, with directions dictated by the external magnetic field. The observation of photoluminescence from all four transitions is consistent with the expected polarization degeneracy of the cavity mode (i.e., if a polarization mode were too spectrally detuned, we would have not observed the two emission lines with polarizations associated with it). We note that the collection of horizontally polarized light is less efficient than that of the vertically polarized light due to a small spectral splitting of polarization modes of this cavity caused by fabrication imperfections. Despite such quantitative differences, the ability to access

quantum dots with light beams orthogonal to each other is crucial for the realization of pulse sequences for coherently controlling the quantum dot spin for quantum information processing utilizing circularly polarized light[91,95,96].

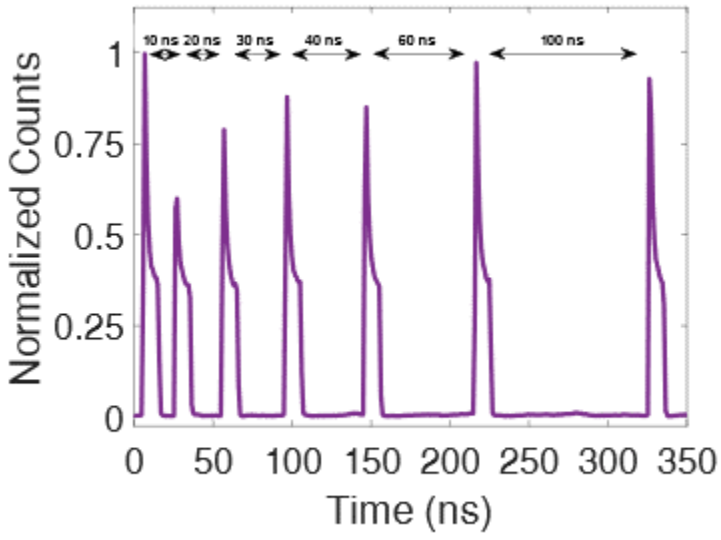

Figure 28 Electron spin relaxation inside a bullseye cavity

To further emphasize the potential of controlling the quantum dot spin in the bullseye cavity, we use laser pulses resonant with one of the optical transitions of the dot to optically pump the spin (under B = 9 T). Varying the free evolution time between these pulses and measuring the emission of Raman signal from the dot results in the saturation behavior depicted in Figure 28. The sharp peak of the Raman signal emitted under the application of the first pulse indicates the optical initialization of the spin to one of its ground states. Then, the application of additional pumping pulses should not induce any Raman signal. Experimentally, however, the pulses induce undesired Raman signals that saturate for the free evolution time of T1 = 21.2 ± 3.5 ns (extracted from the leastsquares fitting shown in the inset of Figure 28). This saturated Raman

signal represents the relaxation of the quantum dot spin, which reduces the spin initialization fidelity down to ~25%.

The observed spin relaxation is dominated by two physical mechanisms. First, the main mechanism that causes spin relaxation is the cotunneling of the electron confined in the dot with the electrons in the n-type back contact,[118] which results in our sample in spin relaxation times of a few tens of nanoseconds even for dots in the bulk. These natural relaxation times can be further extended by orders of magnitude by modifying the tunnel barriers (GaAs layers) of the diode. [118,119] The second (minor) cause for the short spin relaxation time observed here is the spectral proximity of the bullseye cavity (~905 nm) to the wetting layer. Given this spectral proximity, pumping an optical transition of the dot coupled to the cavity may lead to a residual above-band pumping of both spin states, thereby reducing the spin initialization fidelities (by a few additional percent) compared to the those observed for dots with optical wavelengths of ~930 nm. This residual pumping can be mitigated by designing and utilizing bullseye cavities with higher resonant wavelengths: e.g., by increasing the dimensions of the rings. The mitigation of both natural and laser-induced spin relaxation mechanisms could enable high fidelity spin control of the quantum dot spin using low laser powers, thereby upgrading the potential of these dots for quantum information processing.

Chapter 5: Ongoing projects and future directions

We begin this chapter by reiterating some of the requirements for achieving semiconductor cavity QED platforms that are viable for quantum information processing applications:

(i) High cooperativity

(ii) Near unity coupling efficiency to the atom-cavity system

(iii) For spin qubits in a lambda system: large spin lifetimes and coherence times

We have demonstrated that the near Gaussian far field emission pattern of Bullseye cavities can substantially improve the coupling efficiency over the far field pattern of L3 cavities. We also observed a decent cooperativity of 8, which was enabled by the mitigation of charge noise by the p-i-n-i-n diode heterostructures. However, we saw that the spin relaxation time of dots coupled to Bullseye devices was poor, limited to 50ns in most cases. One of the reasons for this limitation is the 30nm tunnel barrier between the quantum dot layer and the back n contact of the diode which forms the Fermi Sea source of electrons for charging the dot.

A limitation of the Bullseye device, from a photonic point of view, is that high efficiency and high cooperativity are somewhat conflicting requirements. Bullseye cavities can be designed with partially etched gratings such that the emission is biased upwards and therefore is more efficiently collected by an objective lens. However, this leads to lower device quality factor, i.e., a higher κ for the cavity, and therefore a lower Cooperativity, all other things being equal.

In this chapter, we try to address both problems. We characterize the spin lifetimes in p-i-n-i-n heterostructures with a sacrificial layer of AlGaAs with 40nm and 50nm tunnel barriers between the quantum dot layer and the back n-contact. We find that 40nm tunnel barriers performed the best given the same growth conditions. This is not in line with previous findings in the literature where 50nm tunnel barrier devices performed better in the case of a Schottky diode [76]. The reason for this inconsistency is not clear as of now.

To address the conflicting requirements between Bullseye efficiency and cooperativity, while also achieving quality factors >1000 that Bullseye cavities are typically limited to in simulation, we investigate nanobeam cavities with adiabatically tapered waveguides. Nanobeam cavities have been shown to have quality factors as high as 25000 for InAs/GaAs quantum dots substrates. [123] Theoretically, the quality factors can be as large as a few million. Adiabatically tapering a waveguide can theoretically yield efficiencies >95%, as we show via means of FDTD simulations. In this chapter, we show the design and simulation results for nanobeam cavities with adiabatically tapered waveguides. We show the developments we have made towards fabricating these devices in p-i-n-i-n diode heterostructures, as well as some device characterization data.

5.1 Dependence of spin lifetime on tunnel barrier for p-i-n-i-n diode heterostructures

Our results in the previous chapter used a device with 30nm tunnel barrier. We observed spin lifetimes below 100ns, which is far below the spin lifetimes observed in Schottky diode heterostructures [76]. To study whether increasing the tunnel barrier is effective in increasing the spin relaxation time as a result of the decrease in cotunneling

rate [76], we characterized the spin lifetimes of electron spins in negatively charged quantum dots in samples with 40nm and 50nm tunnel barriers.

Spin lifetime measurements in p-i-n-i-n diode heterostructures with 40nm tunnel barriers

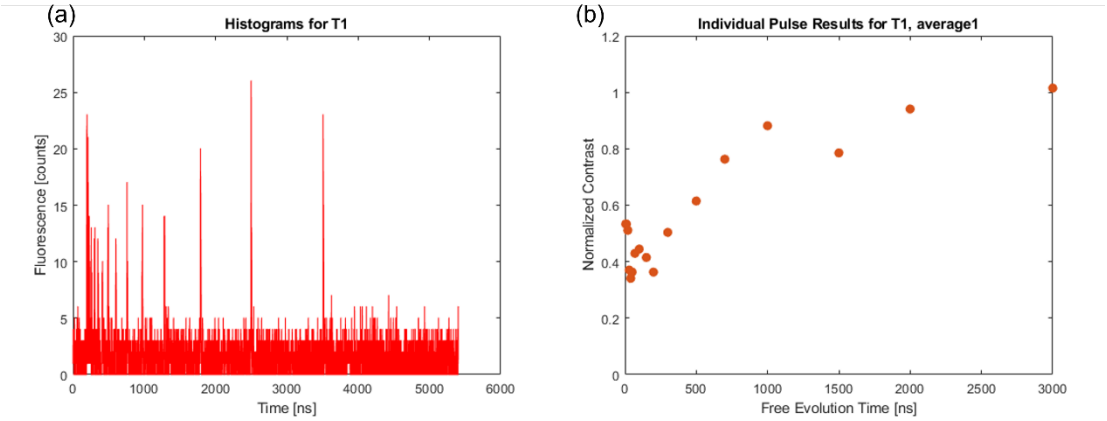

Figure 29 spin lifetime test for 40nm tunnel barrier pinin diode

Figure 29 shows the spin lifetime measurement of electron spin in one negatively charged InAs dot from a sample with a pinin diode heterostructure. Figure 29(a) shows the time resolved photon counts when spin initialization pulses of a duration of 10ns are applied with time delays to capture the spin relaxation time response. After the fluorescence due to the first initialization pulse, the fluorescence from the application of the subsequent pulses is suppressed due to optical spin pumping [93]. As the spin relaxes to thermal equilibrium, we observe fluorescence levels similar to that of the first pulse in the sequence. It can be seen from figure 29(b) that it takes about 3us for the spin to fully relax. This corresponds to a spin relaxation time of about 600ns, which is representative of other dots in the sample and better than what we observed for the

30nm tunnel barrier sample. We ascribe this improvement to the reduced co-tunneling rate due to the increased length of the tunnel barrier. [76]

Spin lifetime measurements in p-i-n-i-n diode heterostructures with 50nm tunnel barriers

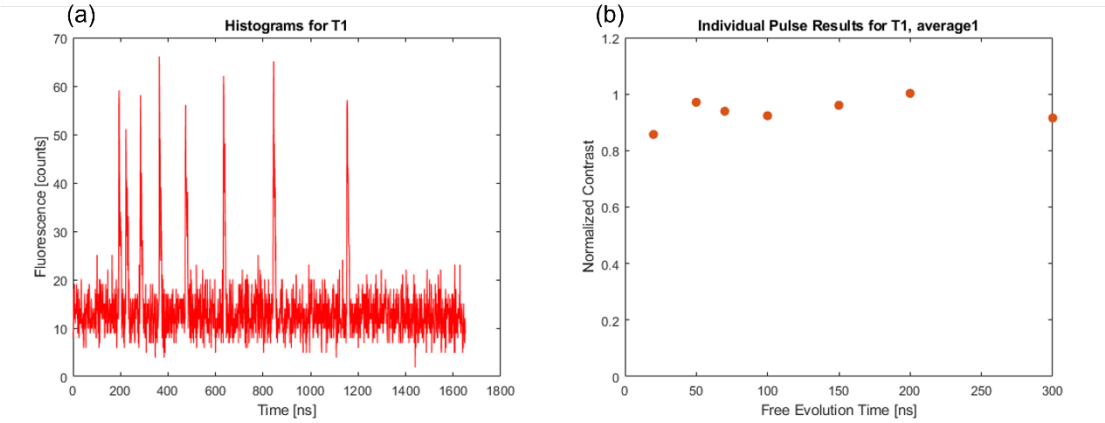

Figure 30 Spin lifetime test for 50nm tunnel barrier pinin diode

Figure 30 shows a spin relaxation measurement like the one in the previous subsection. In this case, the dot is embedded in a diode structure with a tunnel barrier of 50nm width. This measurement is representative of the measurement performed on other dots on the sample. Contrary to our expectations, the spin relaxation time in these samples was rather poor. In the example shown by the figure above, the spin relaxation is happening on the order of 10s of nanoseconds.

5.2 Nanobeam cavities with adiabatic tapers

Adiabatically tapering a single mode waveguide

The idea of adiabatic tapering is simple. We start with the width of a single mode waveguide. We taper the mode slow enough such that the mode stays guided, while the

effective index of the mode decreases. As the refractive index of the mode approaches 1, the taper can be terminated as now the waveguide mode is nearly impedance matched with vacuum and transmits through the waveguide into vacuum with low reflection or scattering loss.

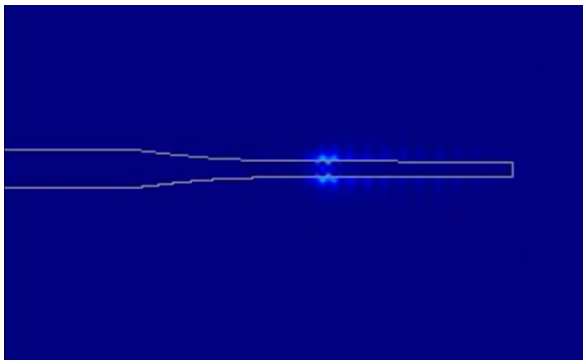

Figure 31 Nonlinear adiabatic taper

Figure 31 shows the design of an adiabatic taper based on the adiabatic condition for GaAs. The figure is a snapshot of the movie generated from Lumerical FDTD which shows the propagation of the electric field along the waveguide when excited by a Mode Source. The adiabatic condition is given by:

$$\frac{dw}{dz} \ll (n_{eff}(w) - 1) \qquad ()$$

where w is the width of the waveguide at location z, z=0 being the beginning of the taper. This differential equation gives rise to a highly nonlinear taper. Since the refractive index of GaAs @920nm is ~3.5>>1, the initial taper happens very fast. This can give rise to short tapers which are convenient for working with short working distance objectives.

The following table shows a comparison between linear and nonlinear tapers of length 9.4um designed for a GaAs waveguide of width 300nm at a wavelength of 920nm. The different columns of the table show the fraction of the source light that gets emitted into a certain NA. As the table clearly shows, the nonlinear taper designed using the adiabatic condition outperforms the linear taper.

Taper type	**NA = 0.34 Transmission**	**NA = 0.5 Transmission**	**NA = 0.7 Transmission**
Linear	0.47	0.77	0.95
Non-Linear	0.79	0.92	0.97

Nanobeam cavity design

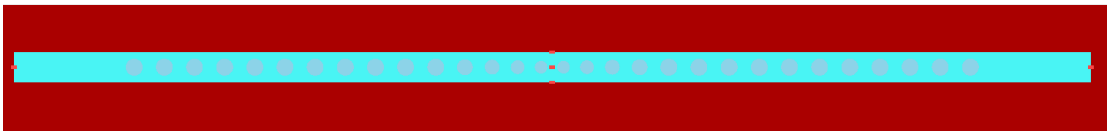

Figure 32 Nanobeam cavity with adiabatically tapered central holes

The nanobeam cavity design is based on a 1D photonic crystal with a central defect, as shown in the figure above. Note that the hole size and period is tapered towards the center of the cavity. This is to ensure that the Bloch modes of the photonic crystal mirrors are adiabatically transformed into the mode of the waveguide as they approach the cavity defect. This prevents any unwanted scattering and enables a high Q cavity design. For the design above, we simulated a cavity Q of 1.9 million at the design wavelength of 940nm. The calculated mode volume of the cavity is $0.16\left(\frac{\lambda}{n}\right)^3$, where n=3.55 is the refractive index of GaAs.

Fabricated one sided nanobeam cavities with adiabatic tapers.

In order to make one sided nanobeam cavities, we reduce the number of holes of the photonic crystal mirror on the side which is close to the adiabatic tapers. We fabricated these devices on our pinin diode heterostructure samples. The following picture shows an SEM image of the fabricated cavities after etching and undercut + precision cleaving.

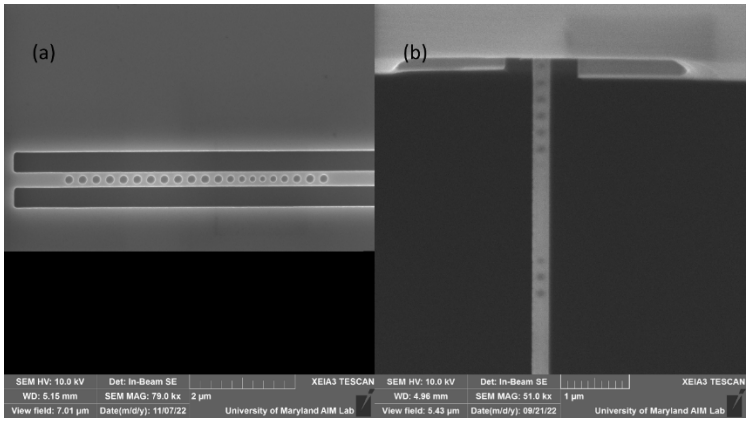

Figure 33 Fabricated nanobeam cavities

Characterization of fabricated cavities at room temperature

Figure 34 Schematic of nanobeam measurement with lensed fibers

The figure above shows a schematic of the optical setup that we use to characterize the nanobeam cavities. The laser light exiting out of the lensed fiber falls on the tapered nanobeam cavity. The reflected light from the nanobeam cavity is collected into the

lensed fiber. The reflected light is then imaged on a spectrometer CCD to measure the reflection spectrum of the nanobeam cavity.

The figure below shows the reflection spectra of two of the nanobeam cavities characterized at room temperature. We observe a dip at the resonance wavelength of the fundamental mode of the cavity. The dip in the reflection spectrum occurs close to the design wavelength of 940nm in both bases. We obtain a cavity Q of ~2000 via a Lorentzian fit.

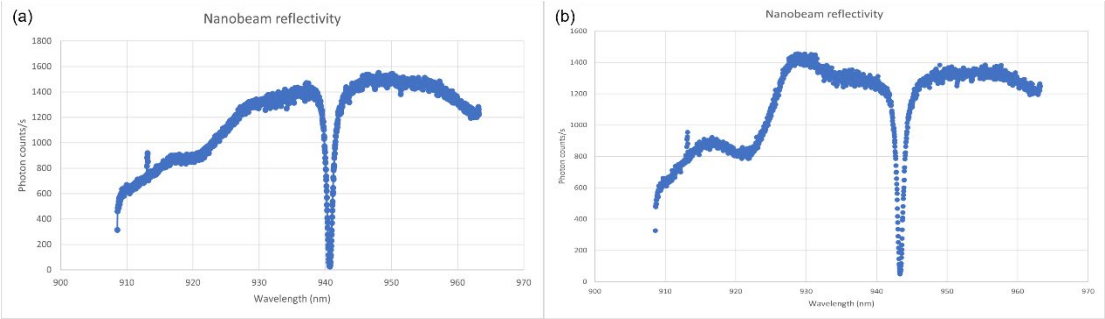

Figure 35 Dip in nanobeam reflectivity at cavity resonance

5.3 Outlook

In order to obtain InAs/GaAs quantum dots in pinin diodes with lifetimes comparable to Schottky diodes, we will keep working with our collaborators to figure out where the issues are. Another alternative is to investigate GaAs/AlGaAs quantum dots, which have larger spin coherence times due to lower strain.

We need to optimize the fabrication of nanobeam cavities in order to obtain higher quality factors. We are working on ebeam lithography with a Silicon Nitride hard mask which is more resistant to etching under a chlorine plasma and would allow longer etch times such that the cavity holes are etched through.

Appendices

Appendix 2.A: Derivation of Scattering Amplitudes

To calculate the scattering amplitudes, we note:

$$\begin{aligned}\psi_{\mathrm{pq}}(\tau_1,\tau_2) &= \langle 0|\,\hat{p}_{\mathrm{out}}(\tau_2)\hat{q}_{\mathrm{out}}(\tau_1)\,|\Psi_{\mathrm{in}}\rangle \\ &= \int_{-\infty}^{\infty} \mathrm{d}t_1 \int_{t_1}^{\infty} \mathrm{d}t_2\; \xi(t_1,t_2) G_{\mathrm{pq}}(\tau_1,\tau_2;t_1,t_2)\end{aligned} \tag{2A.1}$$

where

$$G_{\mathrm{pq}}(\tau_1,\tau_2;t_1,t_2) = \langle 0|\,\hat{p}_{out}(\tau_2)\hat{q}_{out}(\tau_1)\hat{a}^{\dagger}_{\mathrm{in}}(t_1)\hat{a}^{\dagger}_{\mathrm{in}}(t_2)\,|0\rangle \tag{2A.2}$$

Therefore, to calculate the desired scattering amplitudes pq, we first calculate G_{pq} and then use eq. 2A.1. In order to calculate G_{pq}, we first recall the result from ref. [14] that will be used repeatedly in this section. Throughout this section the time orderings $t_2 \geq t_1$ and $\tau_2 \geq \tau_1$ are assumed.

$$\langle 0|\,\sigma(\tau_1)\sigma^{\dagger}(t_1)\,|0\rangle = \langle 0|\,\tilde{\sigma}(\tau_1)\tilde{\sigma}^{\dagger}(t_1)\,|0\rangle \tag{2A3.a}$$

$$\begin{aligned}&\langle 0|\,\sigma(\tau_1)\sigma(\tau_2)\sigma^{\dagger}(t_2)\sigma^{\dagger}(t_1)\,|0\rangle = \\ &\qquad \langle 0|\,\tilde{\sigma}(\tau_1)\tilde{\sigma}(\tau_2)\tilde{\sigma}^{\dagger}(t_2)\tilde{\sigma}^{\dagger}(t_1)\,|0\rangle\end{aligned} \tag{2A3.b}$$

with

$$\tilde{\sigma}(t) = e^{i\hat{H}_{\mathrm{eff}}t}\hat{\sigma}e^{-i\hat{H}_{\mathrm{eff}}t} \tag{2A.4}$$

where

$$\hat{H}_{\mathrm{eff}} = -2i\gamma\hat{\sigma}^{\dagger}\hat{\sigma} \tag{2A.5}$$

Using eqs. (2A.4) and (2A.5) and the properties of the operators σ and σ^+, we can calculate the amplitudes corresponding to eqs 2A.3. In Eq. 2A.3a, $\tau_1 \geq t_1$ is the only possible time ordering because the atom must be raised to the excited state before it is lowered to the ground state. In Eq. 2A.3a, $\tau_2 \geq t_2 \geq \tau_1 \geq t_1$ is the only possible ordering, because before being raised by $\sigma^+(t_2)$,the atom must be lowered. Therefore, we have:

$$\langle 0|\, \hat{\sigma}(\tau_1)\hat{\sigma}^\dagger(t_1)\, |0\rangle = e^{-2\gamma(\tau_1 - t_1)}\Theta(\tau_1 - t_1) \tag{2A.6a}$$

$$\begin{aligned}\langle 0|\, \hat{\sigma}(\tau_1)\hat{\sigma}(\tau_2)\hat{\sigma}^\dagger(t_2)\hat{\sigma}^\dagger(t_1)\, |0\rangle = \\ e^{-2\gamma(\tau_2 - t_2)}e^{-2\gamma(\tau_1 - t_1)}\times \\ \Theta(\tau_2 - t_2)\Theta(\tau_2 - t_1)\Theta(\tau_1 - t_1)\end{aligned} \tag{2A.6b}$$

where Θ is the Heaviside step function and ensures the time orderings.

Before we proceed to the calculations of G_{pq}, we also recall the quantum causality conditions

$$\left[\hat{\sigma}(t), \hat{I}(\tau)\right] = \left[\hat{\sigma}^\dagger(t), \hat{I}(\tau)\right] = 0, \text{for } t \leq \tau \tag{2A.7a}$$

$$\left[\hat{\sigma}(t), \hat{O}(\tau)\right] = \left[\hat{\sigma}^\dagger(t), \hat{O}(\tau)\right] = 0, \text{for } t \geq \tau \tag{2A.7b}$$

where $\hat{I}$ stands for input annihilation or raising operators, and $\hat{O}$ stands for output annihilation or raising operators.

We first calculate the scattering amplitudes for two reflection events G_{bb}, which gives:

$$\begin{aligned}\langle 0|\, b_{out}(\tau_2)b_{out}(\tau_1)a_{in}^\dagger(t_1)a_{in}^\dagger(t_2)\, |0\rangle = \\ 2\gamma\, \langle 0|\, \sigma(\tau_2)\sigma(\tau_1)a_{in}^\dagger(t_1)a_{in}^\dagger(t_2)\, |0\rangle\end{aligned} \tag{2A.8}$$

We first note here that the only time ordering which gives a non-zero result is $\tau_2 \geq t_2 \geq \tau_1 \geq t_1$. This is because other possible time orderings of eqn (2A.8) result in 0. Therefore, we have:

$$\begin{aligned} G_{\mathrm{bb}} = 2\gamma \langle 0| \sigma(t_2) a_{in}^{\dagger} \tau_2) \sigma(t_1) a_{in}^{\dagger}(\tau_1) |0\rangle = \\ 4\gamma^2 \langle 0| \sigma(t_2) \sigma^{\dagger}(\tau_2) \sigma(t_1) \sigma^{\dagger}(\tau_1) |0\rangle = \\ 4\gamma^2 e^{-2\gamma(t_2-\tau_2)} e^{-2\gamma(t_1-\tau_2)} \times \\ \Theta(t_2-\tau_2)\Theta(\tau_2-t_1)\Theta(t_1-\tau_1) \end{aligned} \tag{2A.9}$$

where the first step follows from applying the causality condition (2A.7a) on the result of eqn. (2A.8). The second step follows from using $a_{in}(t) = a_{out}(t) + \sqrt{2\gamma}\sigma^{+}(t)$ and the causality condition (2A.7b) and the last step follows from eqn. (2A.6b).

Using the result for G_{bb} in eqn. (2A.1), we obtain:

$$\begin{aligned} \psi_{\mathrm{bb}}(\tau_1, \tau_2) = 4\gamma^2 e^{-2\gamma(\tau_1+\tau_2)} \times \\ \int_{\tau_1}^{\tau_2} \mathrm{d}\tau_2 \int_{-\infty}^{\tau_1} \mathrm{d}t_1 e^{2\gamma(t_1+t_2)} \xi(t_1, t_2) \end{aligned} \tag{2A.10}$$

To obtain G_{ba}, we observe:

$$\begin{aligned} G_{\mathrm{ab}} = \langle 0| a_{out}(t_2) b_{out}(t_1) a_{in}^{\dagger}(\tau_1) a_{in}^{\dagger}(\tau_2) |0\rangle = \\ -\sqrt{2\gamma} \langle 0| a_{in}(t_2) \sigma(t_1) a_{in}^{\dagger}(\tau_1) a_{in}^{\dagger}(\tau_2) |0\rangle \\ + 2\gamma \langle 0| \sigma(t_2) \sigma(t_1) a_{in}^{\dagger}(\tau_1) a_{in}^{\dagger}(\tau_2) |0\rangle \end{aligned} \tag{2A.11}$$

where the equality follows from the input-output relations. We note that the second term on the right-hand side of the equality is G_{bb}. Therefore, we only need to calculate the first term. Using the causality conditions (2A.7a), (2A.7b) and the relation $a_{in}^{+} = a_{out}^{+} + \sqrt{2\gamma}\sigma^{+}(t)$,we get:

$$\langle 0|\, a_{\rm in}(t_2)\sigma(t_1)a_{\rm in}^{\dagger}(\tau_1)a_{\rm in}^{\dagger}(\tau_2)\,|0\rangle = e^{-2\gamma(t_1-\tau_1)}\Theta(t_1-\tau_1)\delta(t_2-\tau_2) \tag{2A.12}$$

plugging this result in eqn (2A.11), we obtain G_{ba}. Now we use eqn. (2A.1) to obtain:

$$\psi_{\rm ba}(\tau_1,\tau_2) = -2\gamma e^{-2\gamma\tau_1}\times \int_{-\infty}^{\tau_1} {\rm d}t_1\, e^{2\gamma t_1}\xi(t_1,\tau_2) + \psi_{\rm bb} \tag{2A.13}$$

Appendix 2.B: Calculation of Routing Efficiency

We can calculate the splitting efficiency from the scattering amplitudes derived in the previous section. To do this, we first calculate the scattering amplitudes at the output of the MZI namely, ψ_{cc}, ψ_{cd}, ψ_{dc}, ψ_{dd}. The probability density of splitting is then given by $\rho_s = |\psi_{cd}|^2 + |\psi_{dc}|^2$.

To calculate the scattering amplitudes at the output of the MZI, we use the MZI input-output relations to express them in terms of the scattering amplitudes at the output of the TLA. We illustrate this procedure by showing the steps for calculating ψ_{cd} explicitly.

$$\begin{aligned}\psi_{\rm cd} = \langle 0|\, \hat{d}_{\rm out}(\tau_2)\hat{c}_{\rm out}(\tau_1)\,|0\rangle &= \langle 0|\, (e^{i\phi}\cos(\theta/2)\hat{a}_{\rm out}(\tau_2) - \sin(\theta/2)\hat{b}_{\rm out}(\tau_2))(e^{i\phi}\sin(\theta/2)\hat{a}_{\rm out}(\tau_1) + \cos(\theta/2)\hat{b}_{\rm out}(\tau_1))\,|0\rangle \\ &= -\sin(\theta/2)\cos(\theta/2)\psi_{\rm rr} + e^{i\phi}\cos^2(\theta/2)\psi_{\rm rt} - e^{i\phi}\sin^2(\theta/2)\psi_{\rm tr} + e^{2i\phi}\sin(\theta/2)\cos(\theta/2)\psi_{\rm tt}\end{aligned} \tag{2B.1}$$

where the first step follows from the definition of ψ_{cd}. The second step follows from the MZI input-output relations. The third step uses the definition of the scattering amplitudes at the output of the TLA. Using the above procedure, we get,

$$\psi_{\rm dc} = -\sin(\theta/2)\cos(\theta/2)\psi_{\rm rr} - e^{i\phi}\sin^2(\theta/2)\psi_{\rm rt} + e^{i\phi}\cos^2(\theta/2)\psi_{\rm tr} + e^{2i\phi}\sin(\theta/2)\cos(\theta/2)\psi_{\rm tt} \tag{2B.2}$$

$$\psi_{cc} = \cos^2(\theta/2)\psi_{rr} + e^{i\phi}\sin(\theta/2)\cos(\theta/2)\psi_{rt} + e^{i\phi}\sin(\theta/2)\cos(\theta/2)\psi_{tr} + e^{2i\phi}\sin^2(\theta/2)\psi_{tt} \tag{2B.3}$$

$$\psi_{dd} = \sin^2(\theta/2)\psi_{rr} - e^{i\phi}\sin(\theta/2)\cos(\theta/2)\psi_{rt} - e^{i\phi}\sin(\theta/2)\cos(\theta/2)\psi_{tr} + e^{2i\phi}\cos^2(\theta/2)\psi_{tt} \tag{2B.4}$$

We note that $|\psi_{cc}|^2 + |\psi_{cd}|^2 + |\psi_{dc}|^2 + |\psi_{dd}|^2 = |\psi_{bb}|^2 + |\psi_{ba}|^2 + |\psi_{ab}|^2 + |\psi_{aa}|^2$. Since the right-hand side of this equation integrates to 1 over the output times τ_1 and τ_2, so does the left-hand side, ensuring proper normalization of the output photon wavefunction. This preservation of probabilities is ensured by the unitarity of the MZI transformation of eq. (7). We obtain the probability density of the two input photons being split to different output modes of the MZI as $\rho_s = |\psi_{cd}|^2 + |\psi_{dc}|^2$, which gives:

$$\rho_s = \frac{1}{4}(2\psi_{bb}\left(-\sin(4\omega)\cos(\phi)(\psi_{ba}+\psi_{ab}) - 8\sin^2(\omega)\cos^2(\omega)\cos(2\phi)\psi_{aa}\right) + 2\sin^2(2\omega)\psi_{bb}^2 + 2\psi_{ba}((\cos(4\omega)-1)\psi_{ab} + \sin(4\omega)\cos(\phi)\psi_{aa}) + (\cos(4\omega)+3)\psi_{ba}^2 + 2\sin(4\omega)\cos(\phi)\psi_{ab}\psi_{aa} + (\cos(4\omega)+3)\psi_{ab}^2 + 2\sin^2(2\omega)\psi_{aa}^2) \tag{2B.5}$$

The routing efficiency is given by the integral of ρ_s over t and τ.

Appendix 2.C: Routing efficiency for uncorrelated exponential inputs

The input state of two uncorrelated photons with an exponential pulse profile is given by $\xi(t_1, t_2) = \sqrt{2}\xi(t_1)\xi(t_2)$ with $\xi(t) = \sqrt{2\kappa}e^{-\kappa t}$. Plugging this input state into eqns. (10) yields the following expressions for the two photon wavefunctions at the outputs $\mathbf{a_{out}}$ and $\mathbf{b_{out}}$ of the two-level atom:

$$\psi_{bb}(\tau_1, \tau_2) = -\frac{8\sqrt{2}\gamma^2\kappa\left(e^{2\gamma\tau_1} - e^{\kappa\tau_1}\right)e^{-2\tau_1(\gamma+\kappa)-\tau_2(2\gamma+\kappa)}\left(e^{2\gamma\tau_1+\kappa\tau_2} - e^{\kappa\tau_1+2\gamma\tau_2}\right)}{(\kappa-2\gamma)^2} \tag{2C.1a}$$

$$\psi_{ba}(\tau_1, \tau_2) = -\frac{4\sqrt{2}\gamma\kappa\left(e^{2\gamma\tau_1} - e^{\kappa\tau_1}\right)e^{-2\tau_1(\gamma+\kappa)-\tau_2(2\gamma+\kappa)}\left(2\gamma e^{2\gamma\tau_1+\kappa\tau_2} - \kappa e^{\kappa\tau_1+2\gamma\tau_2}\right)}{(\kappa-2\gamma)^2} \tag{2C.1b}$$

$$\psi_{ab}(\tau_1, \tau_2) = \frac{4\sqrt{2}\gamma\kappa e^{-2\tau_1(\gamma+\kappa)-\tau_2(4\gamma+\kappa)}\left(-2\gamma e^{2\kappa\tau_1+4\gamma\tau_2} - 2\gamma e^{4\gamma\tau_1+2\gamma\tau_2+\kappa\tau_2} + (4\gamma-\kappa)e^{(2\gamma+\kappa)(\tau_1+\tau_2)} + \kappa e^{2\gamma\tau_1+\kappa\tau_1+4\gamma\tau_2}\right)}{(\kappa-2\gamma)^2} \tag{2C.1c}$$

$$\psi_{aa} = \xi(\tau_1, \tau_2) + \psi_{ab}(\tau_1, \tau_2) + \psi_{ba}(\tau_1, \tau_2) - \psi_{bb}(\tau_1, \tau_2) \tag{2C.1d}$$

Using these expressions in eqn. 2B.5, we can calculate probability density that the two input photons are routed to different output ports $\mathbf{c_{out}}$ and $\mathbf{d_{out}}$ of the interferometer. Integrating the resulting expression over τ_1 and τ_2 gives the following routing efficiency:

$$P_S = \frac{(\kappa(\kappa(10-3\kappa)+20)-8)\cos(4\omega)+16\kappa\sin^2(2\omega)\cos(2\phi)+32\kappa\sin(4\omega)\cos(\phi)+\kappa(\kappa(3\kappa+38)+44)+8}{4(\kappa+2)^2(3\kappa+2)} \tag{2C.2}$$

Here, we set the atomic bandwidth $\gamma = 1$. Please note that this merely corresponds to expressing the pulse bandwidth κ in the units of the atomic bandwidth γ.

Appendix 2.D: Routing efficiency for entangled exponential inputs

The input state of two entangled photons with an exponential pulse profile is given by $\xi(t_1, t_2) = 2\sqrt{\kappa\delta}\, e^{-\kappa t_1}\, e^{-\delta(t_2-t_1)}$. We follow the same steps as in the previous section to obtain the two-photon wavefunction at the output of the two-level atom. The resulting routing efficiency in the stationary limit is given by:

$$P_S = \frac{-(\delta((\delta-10)\delta-12)+8)\cos(4\omega)+16\delta\sin^2(2\omega)\cos(2\phi)+32\delta\sin(4\omega)\cos(\phi)+\delta(\delta(\delta+22)+20)+8}{4(\delta+2)^3} \tag{2D.1}$$

where the stationary limit corresponds to taking the limit $\kappa \to 0$. Also note that we have set the atomic bandwidth $\gamma = 1$, which merely corresponds to expressing the pulse bandwidth δ in terms of the atomic bandwidth.

Appendix 3.A: Theoretical Model of Bullseye reflectivity spectrum

To calculate the reflectivity spectrum of a bullseye cavity coupled to a neutral quantum dot exciton in the absence of an external magnetic field [yellow lines in Fig. 26 of the main text], we used a Jaynes Cummings model with losses, coherently driven by a laser field. Considering this model, the system Hamiltonian, in the rotating frame with respect to the driving field and under the rotating wave approximation, is given by:

$$\hat{H} = \hbar[(\omega_c - \omega_l)\hat{a}^\dagger\hat{a} + (\omega_a - \omega_l)\hat{\sigma}_+\hat{\sigma}_- + ig(\hat{a}\hat{\sigma}_+ - \hat{a}^\dagger\hat{\sigma}_-) + \xi(\hat{a} + \hat{a}^\dagger)] \tag{3A.1}$$

where g represents the coupling strength of the quantum dot to the cavity, ω_l and ξ represent the frequency and amplitude of the laser, respectively, $a^\dagger$ and a (σ_+ and σ_-) are the creation and annihilation operators of the cavity field (quantum dot optical transition), respectively, and ω_c, ω_a are the resonant frequencies of the cavity and quantum dot, respectively. In addition to the Hamiltonian part, we modeled the losses of photons in the system due to the decay of the cavity field at a rate of κ and the spontaneous emission from the neutral quantum dot exciton at a rate of γ_l by the collapse operators $L_c = \sqrt{\kappa}a$ and $L_a = \sqrt{\gamma}\sigma_-$, respectively. Finally, we modeled the pure Markovian dephasing of the neutral quantum dot exciton at a rate of γ_d by the jump operator $L_d = \sqrt{\gamma_d}\sigma_x$, where σ_x is the x-Pauli operator in the energy subspace of the quantum dot.

To simulate the reflectivity from the cavity [red line in Fig. 26 (a) of the main text], we first used a quantum optics (QuTip) toolbox to calculate the steady-state density matrix, ρ, by solving the Lindblad master equation:

$$\dot{\rho} = -\frac{i}{\hbar}[H, \rho] + \sum_i \left(L_i \rho L_i^\dagger - \frac{1}{2} \left\{ L_i^\dagger L_i, \rho \right\} \right) \tag{3A.2}$$

with i ∈ {c, a, d}. Using the obtained density matrix, we then calculated the steady state cavity field (directly proportional to the cavity reflectivity) given by $n_c = tr(\rho a^\dagger a)$. Repeating the simulation while sweeping the frequency of the laser, ω_l, resulted in the cavity reflectivity spectrum. Figure 26(a) of the main text shows such a reflectivity spectrum driven by a laser with power as low as 0.5 nW, which corresponds to the weak excitation limit $\xi \ll g, \kappa, \gamma_1, \gamma_d$. To properly simulate the spectrum within this limit, we considered a sufficiently low value of ξ and known values of κ = 310 GHz (extracted from the bandwidth of the cavity) and γ_1 = 0.1 GHz (taken from a previous study that used the same wafer 1)), and swept the unknown parameters γ_d and g. By fitting the simulated spectra to the experimental results [blue data points in Fig. 26 (a)], we extracted the parameters of our system, g = 35 GHz and γ_d = 1 GHz. These numbers correspond to a cooperativity of $C \approx \frac{2g^2}{\kappa\gamma_d} \approx 8$.

Fitting the simulation results to the experimental data can also provide an estimate for the efficiency of the optical interface provided by the bullseye cavity. Figure 26(b) of the main text shows both experimentally measured (blue data points) and theoretically simulated (red line) trends of the normalized reflectivity of the cavity as a function of the laser power. The experimental data represent the measured reflectivity of the dip while sweeping the laser power before the sample, P_{in}, normalized by the reflectivity of the cavity in the absence of the quantum dot (observed after changing the voltage bias of the diode). To obtain the simulated results, we solved equation (2) for $\omega_l = \omega_c$ while sweeping the parameter ξ that represents the amplitude of the laser. We

performed this simulation twice, in the presence and absence of the quantum dot (i.e., considering g = 0), which resulted in the steady-state cavity fields $n_c(\xi)$ and $n_0(\xi)$, respectively. From these cavity fields, we finally calculated the normalized reflectivity, $R = \frac{nc}{n0}$. While the input laser power cannot be determined solely from the simulation, this power is directly proportional to the reflectivity in the absence of the quantum dot.

$$\frac{\kappa\hbar\omega_c n_c}{P_{in}} = \eta \tag{3C.3}$$

where η is the efficiency of the optical interface provided by the cavity. As such, fitting the trend of the simulated reflectivity as a function of n_0 to the experimental results allowed us to extract the optical efficiency provided by the cavity, η ≈ 8%, and to present the simulated in Fig. 26(b) in units of μW that represent the laser input power. While the parameters of the simulation were swept to optimally fit the experimental measurements, there are still quantitative discrepancies between theory and experiment. Most notably, the theoretical reflectivity spectrum [red line in Fig. 26 (a)] deviates from the experimental obtained one [blue data points in Fig. 26 (a)], which exhibits a rather asymmetric pattern (Fano resonance). We believe that this observation can be related either to the small non-degeneracy between two orthogonal linearly polarized modes of the particular bullseye cavity, or to an additional interference effect resulting from the Fabry-Perot cavity that constitutes the membrane of our sample. To examine these effects, we measure the photoluminescence signal emitted from the bullseye cavity under above-band excitation in absence of the quantum dot, while separately filtering the two orthogonal polarization modes using quarter and half

waveplates. Figure 36 illustrates the observed small spectral deviation between the polarization modes, as well as the oscillating reflectivity signal associated with Fabry-Perot interference.

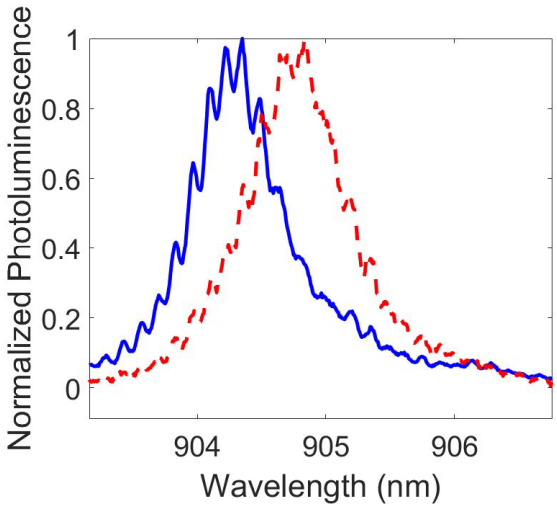

Figure 36 The photoluminescence spectra emitted from two orthogonal linearly polarized modes of the cavity corresponding to figure 26 under above band excitation

Bibliography

1. A. Aspuru-Guzik and P. Walther, Photonic quantum simulators, Nature physics 8, 285 (2012).
2. J. Wang, F. Sciarrino, A. Laing, and M. G. Thompson, Integrated photonic quantum technologies, Nature Photonics 14, 273 (2020).
3. D. E. Chang, V. Vuleti´c, and M. D. Lukin, Quantum nonlinear optics—photon by photon, Nature Photonics 8, 685 (2014).
4. R. Uppu, L. Midolo, X. Zhou, J. Carolan, and P. Lodahl, Quantum-dot-based deterministic photon–emitter interfaces for scalable photonic quantum technology, Nature nanotechnology 16, 1308 (2021).
5. A. W. Elshaari, W. Pernice, K. Srinivasan, O. Benson, and V. Zwiller, Hybrid integrated quantum photonic circuits, Nature Photonics 14, 285 (2020).
6. J. Carolan, C. Harrold, C. Sparrow, E. Mart´ın-L´opez, N. J. Russell, J. W. Silverstone, P. J. Shadbolt, N. Matsuda, M. Oguma, M. Itoh, et al., Universal linear optics, Science 349, 711 (2015).
7. C. Sparrow, E. Mart´ın-L´opez, N. Maraviglia, A. Neville,C. Harrold, J. Carolan, Y. N. Joglekar, T. Hashimoto,N. Matsuda, J. L. O'Brien, et al., Simulating the vibrational quantum dynamics of molecules using photonics, Nature 557, 660 (2018).
8. D. Bunandar, A. Lentine, C. Lee, H. Cai, C. M. Long, N. Boynton, N. Martinez, C. DeRose, C. Chen, M. Grein, et al., Metropolitan quantum key distribution with silicon photonics, Physical Review X 8, 021009 (2018).
9. X. Qiang, X. Zhou, J. Wang, C. M. Wilkes, T. Loke, S. O'Gara, L. Kling, G. D. Marshall, R. Santagati, T. C. Ralph, et al., Large-scale silicon quantum photonics implementing arbitrary two-qubit processing, Nature Photonics 12, 534 (2018).
10. H. Choi, M. Heuck, and D. Englund, Self-similar nanocavity design with ultrasmall mode volume for single-photon nonlinearities, Physical Review Letters 118, 223605 (2017).
11. M. Heuck, K. Jacobs, and D. R. Englund, Photon-photon interactions in dynamically coupled cavities, Physical Review A 101, 042322 (2020).
12. S. Krastanov, M. Heuck, J. H. Shapiro, P. Narang, D. R. Englund, and K. Jacobs, Room-temperature photonic logical qubits via second-order nonlinearities, Nature communications 12, 1 (2021).
13. H. J. Kimble, Strong interactions of single atoms and photons in cavity qed, Physica Scripta 1998, 127 (1998).
14. A. Javadi, I. S¨ollner, M. Arcari, S. L. Hansen, L. Midolo, S. Mahmoodian, G. Kirˇsansk˙e, T. Pregnolato, E. Lee, J. Song, et al., Single-photon non-linear optics with a quantum dot in a waveguide, Nature communications 6,1 (2015).
15. H. L. Jeannic, A. Tiranov, J. Carolan, T. Ramos, Y. Wang, M. H. Appel, S. Scholz, A. D. Wieck, A. Ludwig, N. Rotenberg, et al., Dynamical photon–photon interaction mediated by a quantum emitter, Nature Physics, 1 (2022).

16. S. Fan, S¸. E. Kocaba¸s, and J.-T. Shen, Input-output formalism for few-photon transport in one-dimensional nanophotonic waveguides coupled to a qubit, Physical Review A 82, 063821 (2010).
17. S. Xu and S. Fan, Input-output formalism for few-photon transport: A systematic treatment beyond two photons, Physical Review A 91, 043845 (2015).
18. E. Rephaeli and S. Fan, Dissipation in few-photon waveguide transport, Photonics Research 1, 110 (2013).
19. D. Englund, A. Faraon, I. Fushman, N. Stoltz, P. Petroff, and J. Vu˘ckovi´c, Controlling cavity reflectivity with a single quantum dot, Nature 450, 857 (2007).
20. K. Hennessy, A. Badolato, M. Winger, D. Gerace, M. Atat¨ure, S. Gulde, S. F¨alt, E. L. Hu, and A. Imamo˘glu, Quantum nature of a strongly coupled single quantum dot–cavity system, Nature 445, 896 (2007).
21. K. M. Birnbaum, A. Boca, R. Miller, A. D. Boozer, T. E. Northup, and H. J. Kimble, Photon blockade in an optical cavity with one trapped atom, Nature 436, 87 (2005).
22. A. Rauschenbeutel, G. Nogues, S. Osnaghi, P. Bertet, M. Brune, J.-M. Raimond, and S. Haroche, Coherent operation of a tunable quantum phase gate in cavity qed, Physical Review Letters 83, 5166 (1999).
23. H. Takahashi, E. Kassa, C. Christoforou, and M. Keller, Strong coupling of a single ion to an optical cavity, Physical Review Letters 124, 013602 (2020).
24. A. Wallraff, D. I. Schuster, A. Blais, L. Frunzio, R.-S. Huang, J. Majer, S. Kumar, S. M. Girvin, and R. J. Schoelkopf, Strong coupling of a single photon to a superconducting qubit using circuit quantum electrodynamics, Nature 431, 162 (2004).
25. A. Nysteen, D. P. McCutcheon, M. Heuck, J. Mørk, and D. R. Englund, Limitations of two-level emitters as nonlinearities in two-photon controlled-phase gates, Physical Review A 95, 062304 (2017).
26. T. Ralph, I. S¨ollner, S. Mahmoodian, A. White, and P. Lodahl, Photon sorting, efficient bell measurements, and a deterministic controlled-z gate using a passive two level nonlinearity, Physical Review Letters 114, 173603 (2015).
27. F. Yang, M. M. Lund, T. Pohl, P. Lodahl, and K. Mølmer, Deterministic photon sorting in waveguide qed systems, Physical Review Letters 128, 213603 (2022).
28. S. Rosenblum, S. Parkins, and B. Dayan, Photon routing in cavity qed: Beyond the fundamental limit of photon blockade, Physical Review A 84, 033854 (2011).
29. T. Aoki, A. Parkins, D. Alton, C. Regal, B. Dayan, E. Ostby, K. J. Vahala, and H. Kimble, Efficient routing of single photons by one atom and a microtoroidal cavity, Physical Review Letters 102, 083601 (2009).
30. M. Reck, A. Zeilinger, H. J. Bernstein, and P. Bertani, Experimental realization of any discrete unitary operator, Physical Review Letters 73, 58 (1994).

31. W. R. Clements, P. C. Humphreys, B. J. Metcalf, W. S. Kolthammer, and I. A.Walmsley, Optimal design for universal multiport interferometers, Optica 3, 1460 (2016).
32. J. R. Basani, S. K. Vadlamani, S. Bandyopadhyay, D. R. Englund, and R. Hamerly, A self-similar sine–cosine fractal architecture for multiport interferometers, Nanophotonics 10.1515/nanoph-2022-0525 (2023).
33. E. Knill, R. Laflamme, and G. J. Milburn, A scheme for efficient quantum computation with linear optics, Nature 409, 46 (2001).
34. P. Kok, W. J. Munro, K. Nemoto, T. C. Ralph, J. P. Dowling, and G. J. Milburn, Linear optical quantum computing with photonic qubits, Reviews of Modern Physics 79, 135 (2007).
35. M. O. Scully and M. S. Zubairy, Quantum optics (1999).
36. H. F. Hofmann, K. Kojima, S. Takeuchi, and K. Sasaki, Entanglement and four-wave mixing effects in the dissipation-free nonlinear interaction of two photons at a single atom, Physical Review A 68, 043813 (2003).
37. J.-T. Shen and S. Fan, Strongly correlated multiparticle transport in one dimension through a quantum impurity,Physical Review A 76, 062709 (2007).
38. V. I. Yudson and P. Reineker, Multiphoton scattering in a one-dimensional waveguide with resonant atoms, Physical Review A 78, 052713 (2008).
39. T. Shi and C. Sun, Lehmann-symanzik-zimmermann reduction approach to multiphoton scattering in coupled resonator arrays, Physical Review B 79, 205111 (2009).
40. T. Shi, S. Fan, C. Sun, et al., Two-photon transport in a waveguide coupled to a cavity in a two-level system, Physical Review A 84, 063803 (2011).
41. Bylander, J.; et al. Noise spectroscopy through dynamical decoupling with a superconducting flux qubit. Nat. Phys. 2011, 7, 565−570.
42. Sung, Y.; et al. Multi-level quantum noise spectroscopy. Nat. Commun. 2021, 12, 967
43. Bar-Gill, N.; et al. Suppression of spin-bath dynamics for improved coherence of multi-spin-qubit systems. Nat. Commun. 2012,3, 858
44. Romach, Y.; et al. Measuring Environmental Quantum Noise Exhibiting a Nonmonotonic Spectral Shape. Phys. Rev. Applied 2019, 11, 014064
45. Malinowski, F. K.; et al. Notch filtering the nuclear environment of a spin qubit. Nat. Nanotechnol. 2017, 12, 16−20.
46. Chan, K. W.; et al. Assessment of a Silicon Quantum Dot Spin Qubit Environment via Noise Spectroscopy. Phys. Rev. Applied 2018, 10, 044017.
47. Fuchs, G. D.; Dobrovitski, V. V.; Toyli, D. M.; Heremans, F. J.; Awschalom, D. D. Gigahertz Dynamics of a Strongly Driven Single Quantum Spin. Science 2009, 326, 1520−1522.
48. Froning, F. N. M.; et al. Ultrafast hole spin qubit with gate tunable spin−orbit switch functionality. Nat. Nanotechnol. 2021, 16, 308−312.
49. Bayer, M.; Ortner, G.; Stern, O.; Kuther, A.; Gorbunov, A. A.; Forchel, A.; Hawrylak, P.; Fafard, S.; Hinzer, K.; Reinecke, T. L.; et al. Fine structure of nuclear and charged excitons in self-assembled In(Ga)As/(Al)GaAs quantum dots. Phys. Rev. B 2002, 65, 195315

50. Huber, D.; Reindl, M.; Huo, Y.; Huang, H.; Wildmann, J. S.; Schmidt, O. G.; Rastelli, A.; Trotta, R. Highly indistinguishable and strongly entangled photons from symmetric GaAs quantum dots. Nat. Commun. 2017, 8, 15506
51. Benyoucef, M.; Yacob, M.; Reithmaier, J. P.; Kettler, J.;Michler, P. Telecom-wavlength (1.5 um) single-photon emission from InP-based quantum dots. Appl. Phys. Lett. 2013, 103, 162101.
52. Debroux, R.; Michaels, C. P.; Purser, C. M.; Wan, N.; Trusheim, M. E.; Mertinez, J. A.; Parker, R. A.; Stramma, A. M.; Chen, K. C.; de Santis, L.; et al. Quantum Control of the Tin-Vacancy Spin Qubit in Diamond. Phys. Rev. X 2021, 11, 041041.
53. Kuhlmann, A. V.; et al. Charge noise and spin noise in a semiconductor quantum device. Nat. Phys. 2013, 9, 570−575.
54. Munsch, M.; et al. Resonant driving of a single photon emitter embedded in a mechanical oscillator. Nat. Commun. 2017, 8, 76.
55. Dahbashi, R.; Hubner, J.; Berski, F.; Pierz, K.; Oestreich, M. Optical Spin Noise of a Single Hole Spin Localized in an (InGa)As Quantum Dot. Phys. Rev. Lett. 2014, 112, 156601.

56. Bulutay, C. Quadrupolar spectra of nuclear spins in strained InxGa1-xAs quantum dots. Phys, Rev. B 2012, 85, 115313.
57. Stockill, R.; Gall, C. L.; Matthiesen, C.; Huthmacher, L.; Clarke, E.; Hugues, M.; Atatüre, M. Quantum dot spin coherence governed by a strained nuclear environment. Nat. Commun. 2016, 7,12745.
58. Chekhovich, E. A.; et al. Structural analysis of strained quantum dots using nuclear magnetic resonance. Nat. Nanotechnol. 2012, 7, 646−650.
59. Bulutay, C.; Chekhovich, E. A.; Tartakovskii, A. I. Nuclear magnetic resonance inverse spectra of InGaAs quantum dots: Atomistic level structural information. Phys. Rev. B 2014, 90, 205425.
60. Bodey, J. H.; et al. Optical spin locking of a solid-state qubit. Npj Quantum Inf. 2019, 5, 95.
61. Gangloff, D. A.; et al. Quantum interface of an electron and a nuclear ensemble. Science 2019, 364, 62−66.
62. Meiboom, S.; Gill, D. Modified spin-echo method for measuring nuclear relaxation times. Rev. Sci. Instrum. 1958, 29, 688−691.
63. Kroner, M.; et al. Optical Detection of Single-Electron Spin Resonance in a Quantum Dot. Phys. Rev. Lett. 2008, 100, 156803.
64. Gao, W. B.; Fallahi, P.; Togan, E.; Miguel-Sanchez, J.; Imamoglu, A. Observation of entanglement between a quantum dot spin and a single photon. Nature 2012, 491, 426−430.
65. Ding, X.; He, Y.; Duan, Z.-C.; Gregersen, N.; Chen, M.-C.;Unsleber, S.; Maier, S.; Schneider, C.; Kamp, M.; Höfling, S.; Lu, C.-Y.; Pan, J.-W. On-Demand Single Photons with High Extraction Efficiency and Near-Unity Indistinguishability from a Resonantly Driven Quantum Dot in a Micropillar. Phys. Rev. Lett. 2016, 116,020401.
66. Somaschi, N.; Giesz, V.; De Santis, L.; Loredo, J. C.; Almeida, M. P.; Hornecker, G.; Portalupi, S. L.; Grange, T.; Antón, J.; Demory, C.; et al.

Near-optimal single-photon sources in the solid state. Nat. Photonics 2016, 10, 340.
67. Lodahl, P. Quantum-dot based photonic quantum networks. Quantum. Sci. Technol. 2018, 3, 013001.
68. Schöll, E.; Hanschke, L.; Schweickert, K.; Zeuner, K. D.;Reindl, M.; da Silva, S. F. C.; Lettner, T.; Trotta, R.; Finley, J. J.;Müller, K.; Rastelli, A.; Zwiller, V.; Jöns, K. D. Resonance Fluorescence of GaAs Quantum Dots with Near-Unity Photon Indistinguishability. Nano Lett. 2019, 19, 2404−2410.
69. Tomm, N.; Javadi, A.; Antoniadis, N. O.; Najer, D.; Löbl, M. C.; Korsch, A. R.; Schott, R.; Valentin, S. R.; Wieck, A. D.; Ludwig, A.; Warburton, R. J. A bright and fast source of coherence single photons. Nat. Nanotechnol. 2021, 16, 399−403.
70. Appel, M. H.; et al. Coherent Spin-Photon Interface with Waveguide Induced Cycling Transitions. Phys. Rev. Lett. 2021, 126,013602.
71. Press, D.; et al. Ultrafast optical spin echo in a single quantum dot. Nat. Photonics. 2010, 4, 367−370.
72. Bechtold, A.; Rauch, D.; Li, F.; Simmet, T.; Ardelt, P.-L.; Regler, A.; Muller, K.; Sinitsyn, N. A.; Finley, J. J. Three-stage decoherence dynamics of an electron spin qubit in an optically active quantum dot. Nat. Phys. 2015, 11, 1005−1008.
73. Farfurnik, D.; et al. Optimizing a dynamical decoupling protocol for solid-state electronic spin ensembles in diamond. Phys. Rev. B 2015, 92, 060301.
74. Cywinski, L.; Lutchyn, R. M.; Nave, C. P.; Das Sarma, S. How to enhance dephasing time in superconducting qubits. Phys. Rev. B 2008, 77, 174509.
75. de Sousa, R. Electron Spin Resonance and Related Phenomena in Low-Dimensional Structures; Springer: 2009; Topics in Applied Physics Vol. 115; pp 183−220.
76. Gillard, G.; et al. Fundamental limits of electron and nuclear spin qubit lifetimes in an isolated self-assembled quantum dot. Npj Quantum Inf. 2021, 7, 43.
77. Greilich, A.; Pawlis, A.; Liu, F.; Yugov, O. A.; Yakovlev, D. R.; Lischka, K.; Yamamote, Y.; Bayer, M. Spin dephasing of fluorine bound electrons in ZnSe. Phys. Rev. B 2012, 85, 121303.
78. Santori, C.; Pleton, M.; Solomon, G. S.; Dale, Y.; Yamamoto, Y. Triggered Single Photons from a Quantum Dot. Phys. Rev. Lett. 2001, 86, 1502.
79. Gazzano, O.; de Vasconcellos, S. M.; Arnold, C.; Nowak, A.; Galopin, E.; Sagnes, I.; Lanco, L.; Lemaître, A.; Senellart, P. Bright solid-state sources of indistinguishable single photons. Nat. Commun. 2013, 4, 1425.
80. Ding, X.; He, Y.; Duan, Z.-C.; Gregersen, N.; Chen, M.-C.; Unsleber, S.; Maier, S.; Schneider, C.; Kamp, M.; Höfling, S.; Lu, C.- Y.; Pan, J.-W. On-Demand Single Photons with High Extraction Efficiency and Near-Unity Indistinguishability from a Resonantly Driven Quantum Dot in a Micropillar. Phys. Rev. Lett. 2016, 116,020401.
81. Somaschi, N.; Giesz, V.; De Santis, L.; Loredo, J. C.; Almeida, M.P.; Hornecker, G.; Portalupi, S. L.; Grange, T.; Antón, J.; Demory, C.;et al. Near-optimal single-photon sources in the solid state. Nat. Photonics 2016, 10, 340.

82. Liu, F.; Brash, A. J.; O'Hara, J.; Martins, L. M. P. P.; Phillips, C. L.; Coles, R. J.; Royall, B.; Clarke, E.; Benhtam, C.; Prtljaga, N.; et al. High Purcell factor generation of indistinguishable on-chip single photons. Nat. Nanotechno 2018, 13, 835−840.
83. Schöll, E.; Hanschke, L.; Schweickert, K.; Zeuner, K. D.; Reindl, M.; da Silva, S. F. C.; Lettner, T.; Trotta, R.; Finley, J. J.; Müller, K.; Rastelli, A.; Zwiller, V.; Jöns, K. D. Resonance Fluorescence of GaAs Quantum Dots with Near-Unity Photon Indistinguishability. Nano Lett. 2019, 19, 2404−2410.
84. Wang, H.; He, Y.-M.; Chung, T.-H.; Hu, H.; Yu, Y.; Chen, S.; Ding, X.; Chen, M.-C.; Qin, J.; Yang, X.; et al. Towards optimal single-photon sources from polarized microcavities. Nat. Photonics 2019, 13, 770−775.
85. Tomm, N.; Javadi, A.; Antoniadis, N. O.; Najer, D.; Löbl, M. C.; Korsch, A. R.; Schott, R.; Valentin, S. R.; Wieck, A. D.; Ludwig, A.; Warburton, R. J. A bright and fast source of coherence single photons. Nat. Nanotechnol. 2021, 16, 399−403.
86. Schwartz, I.; Cogan, D.; Schmidgall, E. R.; Don, Y.; Gantz, L.; Kenneth, O.; Lindner, N. H.; Gershoni, D. Deterministic generation of a cluster state of entangled photons. Science 2016, 354, 434−437.
87. Huber, D.; Reindl, M.; Huo, Y.; Huang, H.; Wildmann, J. S.; Schmidt, O. G.; Rastelli, A.; Trotta, R. Highly indistinguishable and strongly entangled photons from symmetric GaAs quantum dots. Nat. Commun. 2017, 8, 15506.
88. Gimeno-Segovia, M.; Rudolph, T.; Economou, S. E. Deterministic Generation of Large-Scale Entangled Photonic Cluster State from Interacting Solid State Emitters. Phys. Rev. Lett. 2019, 123,070501.
89. Istrati, D.; et al. Sequential generation of linear cluster states from a single photon emitter. Nat. Commun. 2020, 11, 5501.
90. Bayer, M.; Ortner, G.; Stern, O.; Kuther, A.; Gorbunov, A. A.; Forchel, A.; Hawrylak, P.; Fafard, S.; Hinzer, K.; Reinecke, T. L.; et al. Fine structure of nuclear and charged excitons in self-assembled In(Ga)As/(Al)GaAs quantum dots. Phys. Rev. B 2002, 65, 195315.
91. Press, D.; Ladd, T. D.; Zhang, B.; Yamamoto, Y. Complete quantum control of a single quantum dot spin using ultrafast optical pulses. Nature (London) 2008, 456, 218.
92. Carter, S. G.; Sweeney, T. M.; Kim, M.; Kim, C. S.; Solenov, D.; Economou, S. E.; Reinecke, T. L.; Yange, K.; Bracker, A. S.; Gammon, D. Quantum control of a spin qubit coupled to a photonic crystal cavity. Nat. Phot. 2013, 7, 329.
93. Warburton, R. J. Single spins in self-assembled quantum dots. Nat. Mater. 2013, 12, 483−493.
94. Bechtold, A.; Rauch, D.; Li, F.; Simmet, T.; Ardelt, P.-L.;Regler, A.; Muller, K.; Sinitsyn, N. A.; Finley, J. J. Three-stage decoherence dynamics of an electron spin qubit in an optically active quantum dot. Nat. Phys. 2015, 11, 1005−1008.
95. Stockill, R.; Gall, C. L.; Matthiesen, C.; Huthmacher, L.; Clarke, E.; Hugues, M.; Atatüre, M. Quantum dot spin coherence governed by a strained nuclear environment. Nat. Commun. 2016, 7,12745.

96. Farfurnik, D.; Singh, H.; Luo, Z.; Bracker, A. S.; Carter, S. G.; Pettit, R. M.; Waks, E. All-optical noise spectroscopy of a solid-state spin. Nano Letters 2023 23 (5), 1781-1786
97. Sun, S.; Kim, H.; Luo, Z.; Solomon, G. H.; Waks, E. A single photon switch and transistor enabled by a solid-state quantum memory. Science 2018, 361, 57−60.
98. Najer, D.; Söllner, I.; Sekatski, P.; Dolique, V.; Löbl, M. C.;Riedel, D.; Schott, R.; Starosielec, S.; Valentin, S. R.; Wieck, A. D.; Sangouard, N.; Ludwig, A.; Warburton, R. J. A gated quantum dot strongly coupled to an optical microcavity. Nature (London) 2019, 575, 622−627.
99. Kimble, H. J. The quantum internet. Nature (London) 2008, 453, 1023−1030.
100. Lodahl, P. Quantum-dot based photonic quantum networks. Quantum. Sci. Technol. 2018, 3, 013001.
101. Luo, Z.; Sun, S.; Karasahin, A.; Bracker, A. S.; Carter, S. G.; Yakes, M. K.; Gammon, D.; Waks, E. A Spin−Photon Interface Using Charge-Tunable Quantum Dots Strongly Coupled to a Cavity. Nano Lett. 2019, 19, 7072−7077.
102. Davanço, M.; Rakher, M. T.; Schuh, D.; Badolato, A.; Srinivasan, K. A circular dielectric grating for vertical extraction of single quantum dot emission. Appl. Phys. Lett. 2011, 99, 041102.
103. Lodahl, P.; Mahmoodian, S.; Stobbe, S. Interfacing single photons and single quantum dots with photonic nanostructures. Rev. Mod. Phys. 2015, 87, 347.
104. Liu, J.; Su, R.; Wei, Y.; Yao, B.; Covre da Silva, S. F.; Yu, Y.; Iles-Smith, J.; Srinivasan, K.; Rastelli, A.; Li, J.; Wang, X. A solid-state source of strongly entangled photon pairs with high brightness and indistinguishability. Nat. Nanotechnol. 2019, 14, 586−593.
105. Kolatschek, S.; Hepp, S.; Sartison, M.; Jetter, M.; Michler, P.; Portalupi, S. L. Deterministic fabrication of circular Bragg gratings coupled to single quantum emitters via the combination of in-situ optical lithography and electron-beam lithography. J. Appl. Phys. 2019, 125, 045701.
106. Moczała-Dusanowska, M.; Dusanowski, L.; Iff, O.; Huber, T.; Kuhn, S.; Czyszanowski, T.; Schneider, C.; Höfling, S. Strain-Tunable Single-Photon Source Based on a Circular Bragg Grating Cavity with Embedded Quantum Dots. ACS Photonics 2020, 7, 3474−3480.
107. Kolatschek, S.; Nawrath, C.; Bauer, S.; Huang, J.; Fischer, J.; Sittig, R.; Jetter, M.; Portalupi, S. L.; Michler, P. Bright Purcell Enhanced Single-Photon Source in the Telecom O-Band Based on a Quantum Dot in a Circular Bragg Grating. Nano Lett. 2021, 21, 7740.
108. Purcell, E. Spontaneous emission probabilities at radio frequencies. Phys. Rev. 1946, 69, 681.
109. Li, L.; Chen, E. H.; Zheng, J.; Mouradian, S. L.; Dolde, F.; Schröder, T.; Karaveli, S.; Markham, M. L.; Twitchen, D. J.; Englund, D. Efficient Photon Collection from a Nitrogen Vacancy Center in a Circular Bullseye Grating. Nano Lett. 2015, 15, 1493−1497.

110. Sapienza, L.; Davanço, M.; Badolato, A.; Srinivasan, K. Nanoscale optical positioning of single quantum dots for bright and pure single-photon emission. Nat. Commun. 2015, 6, 7833.
111. Vora, P. M.; Bracker, A. S.; Carter, S. G.; Sweeney, T. M.; Kim, M.; Kim, C. S.; Yang, L.; Brereton, P. G.; Economou, S. E.; Gammon, D. Spin−cavity interactions between a quantum dot molecule and a photonic crystal cavity. Nat. Commun. 2015, 6, 7665.
112. Löbl, M. C.; Söllner, I.; Javadi, A.; Pregnolato, T.; Schott, R.; Midolo, L.; Kuhlmann, V.; Stobbe, S.; Wieck, A. D.; Lodahl, P.; Ludwig, A.; Warburton, R. J. Narrow optical linewidths and spin pumping on charge-tunable close-to-surface self-assembled quantum dots in an ultrathin diode. Phys. Rev. B 2017, 96, 165440.
113. Waks, E.; Vuckovic, J. Dipole Induced Transparency in Drop-Filter Cavity-Waveguide Systems. Phys. Rev. Lett. 2006, 96, 153601.
114. Fano, U. Effects of Configuration Interaction on Intensities and Phase Shifts. Phys. Rev. 1961, 124, 1866.
115. Rybin, M. V.; Khanikaev, A. B.; Inoue, M.; Samusev, K. B.; Steel, M. J.; Yushin, Y.; Limonov, M. F. Fano Resonance between Mie and Bragg Scattering in Photonic Crystals. Phys. Rev. Lett. 2009, 103, 023901.
116. Limonov, M. F.; Rybin, M. V.; Poddubny, A. N.; Kivshar, Y. S. Fano resonances in photonics. Nat. Photonics 2017, 11, 543.
117. Englund, D.; Fattal, D.; Waks, E.; Solomon, G.; Zhang, B.; Nakaoka, T.; Arakawa, Y.; Yamamoto, Y.; Vuckovi ć, J. Controlling the Spontaneous Emission Rate of Single Quantum Dots in a Two-Dimensional Photonic Crystal. Phys. Rev. Lett. 2005, 95, 013904.
118. Gillard, G.; et al. Fundamental limits of electron and nuclear spin qubit lifetimes in an isolated self-assembled quantum dot. Npj Quantum Inf 2021, 7, 43.
119. Lu, C. Y.; Zhao, Y.; Vamivakas, A. N.; Matthiesen, C.; Fält, S.; Badolato, A.; Atatüre, M. Direct measurement of spin dynamics in InAs/GaAs quantum dots using time-resolved resonance fluorescence. Phys. Rev. B 2010, 81, 035332.
120. D. Pinotsi, P. Fallahi, J. Miguel-Sanchez, and A. Imamoglu, IEEE J. Quantum Electron. 47, 1371 (2011).
121. Midolo, L., Pregnolato, T., Kiršanskė, G., & Stobbe, S. (2015). Soft-mask fabrication of gallium arsenide nanomembranes for integrated quantum photonics. Nanotechnology, 26(48), 484002
122. Hennessy, K., Badolato, A., Winger, M., Gerace, D., Atatüre, M., Gulde, S., ... & Imamoğlu, A. (2007). Quantum nature of a strongly coupled single quantum dot–cavity system. Nature, 445(7130), 896-899.
123. Ohta, R., Ota, Y., Nomura, M., Kumagai, N., Ishida, S., Iwamoto, S., & Arakawa, Y. (2011). Strong coupling between a photonic crystal nanobeam cavity and a single quantum dot. Applied Physics Letters, 98(17), 173104.